

JWST and ALMA Multiple-Line Study in and around a Galaxy at $z = 8.496$: Optical to FIR Line Ratios and the Onset of an Outflow Promoting Ionizing Photon Escape

SEIJI FUJIMOTO,^{1,2,3,*} MASAMI OUCHI,^{4,5,6} KIMHIKO NAKAJIMA,⁴ YUICHI HARIKANE,⁵ YUKI ISOBE,^{5,7}
GABRIEL BRAMMER,^{2,3} MASAMUNE OGURI,^{8,9} CLARA GIMÉNEZ-ARTEAGA,^{2,10} KASPER E. HEINTZ,^{2,11} VASILY KOKOREV,^{2,10}
FRANZ E. BAUER,^{12,13,14} ANDREA FERRARA,¹⁵ TAKASHI KOJIMA,⁵ CLAUDIA DEL P. LAGOS,^{16,17,2} SOMMOVIGO LAURA,¹⁸
DANIEL SCHAEERER,^{19,20} KAZUHIRO SHIMASAKU,^{21,22} BUNYO HATSUKADE,²³ KOTARO KOHNO,^{23,24} FENGWU SUN,²⁵
FRANCESCO VALENTINO,^{2,11,26} DARACH WATSON,^{2,11} YOSHINOBU FUDAMOTO,^{27,28} AKIO K. INOUE,^{27,29}
JORGE GONZÁLEZ-LÓPEZ,^{30,31} ANTON M. KOEKEMOER,³² KIRSTEN KNUDSEN,³³ MINJU M. LEE,^{2,34}
GEORGIOS E. MAGDIS,^{35,36,37} JOHAN RICHARD,³⁸ VICTORIA B. STRAIT,^{2,11} YUMA SUGAHARA,^{39,40} YOICHI TAMURA,⁴¹
SUNE TOFT,^{2,11} HIDEKI UMEHATA,^{42,43} AND GREGORY WALTH⁴⁴

¹Department of Astronomy, The University of Texas at Austin, Austin, TX 78712, USA

²Cosmic Dawn Center (DAWN), Denmark

³Niels Bohr Institute, University of Copenhagen, Lyngbyvej 2, DK2100 Copenhagen Ø, Denmark

⁴National Astronomical Observatory of Japan, 2-21-1 Osawa, Mitaka, Tokyo 181-8588, Japan

⁵Institute for Cosmic Ray Research, The University of Tokyo, 5-1-5 Kashiwanoha, Kashiwa, Chiba 277-8582, Japan

⁶Kavli Institute for the Physics and Mathematics of the Universe (WPI), University of Tokyo, Kashiwa, Chiba 277-8583, Japan

⁷Department of Physics, Graduate School of Science, The University of Tokyo, 7-3-1 Hongo, Bunkyo, Tokyo 113-0033, Japan

⁸Center for Frontier Science, Chiba University, 1-33 Yayoi-cho, Inage-ku, Chiba 263-8522, Japan

⁹Department of Physics, Graduate School of Science, Chiba University, 1-33 Yayoi-Cho, Inage-Ku, Chiba 263-8522, Japan

¹⁰Niels Bohr Institute, University of Copenhagen, Blegdamsvej 17, DK2100 Copenhagen Ø, Denmark

¹¹Niels Bohr Institute, University of Copenhagen, Jagtvej 128, DK-2200 Copenhagen N, Denmark

¹²Instituto de Astrofísica, Facultad de Física, Pontificia Universidad Católica de Chile, Campus San Joaquín, Av. Vicuña Mackenna 4860, Macul Santiago, Chile, 7820436

¹³Centro de Astroingeniería, Facultad de Física, Pontificia Universidad Católica de Chile, Campus San Joaquín, Av. Vicuña Mackenna 4860, Macul Santiago, Chile, 7820436

¹⁴Millennium Institute of Astrophysics, Nuncio Monseñor Sótero Sanz 100, Of 104, Providencia, Santiago, Chile

¹⁵Scuola Normale Superiore, Piazza dei Cavalieri 7, 50126 Pisa, Italy

¹⁶International Centre for Radio Astronomy Research (ICRAR), M468, University of Western Australia, 35 Stirling Hwy, Crawley, WA 6009, Australia.

¹⁷ARC Centre of Excellence for All Sky Astrophysics in 3 Dimensions (ASTRO 3D).

¹⁸Scuola Normale Superiore, Piazza dei Cavalieri 7, 50126 Pisa, Italy

¹⁹Observatoire de Genève, Université de Genève, Chemin Pegasi 51, 1290 Versoix, Switzerland

²⁰CNRS, IRAP, 14 Avenue E. Belin, 31400 Toulouse, France

²¹Department of Astronomy, School of Science, The University of Tokyo, 7-3-1 Hongo, Bunkyo-ku, Tokyo 113-0033, Japan

²²Research Center for the Early Universe, The University of Tokyo, 7-3-1 Hongo, Bunkyo-ku, Tokyo 113-0033, Japan

²³Institute of Astronomy, Graduate School of Science, The University of Tokyo, 2-21-1 Osawa, Mitaka, Tokyo 181-0015, Japan

²⁴Research Center for the Early Universe, Graduate School of Science, The University of Tokyo, 7-3-1 Hongo, Bunkyo-ku, Tokyo 113-0033, Japan

²⁵Steward Observatory, University of Arizona, 933 N. Cherry Avenue, Tucson, AZ 85721, USA

²⁶European Southern Observatory, Karl-Schwarzschild-Str. 2, D-85748 Garching bei Munchen, Germany

²⁷Waseda Research Institute for Science and Engineering, Faculty of Science and Engineering, Waseda University, 3-4-1 Okubo, Shinjuku, Tokyo 169-8555, Japan

²⁸National Astronomical Observatory of Japan, 2-21-1, Osawa, Mitaka, Tokyo, Japan

²⁹Department of Physics, School of Advanced Science Engineering, Faculty of Science and Engineering, Waseda University, 3-4-1 Okubo, Shinjuku, Tokyo 169-8555, Japan

³⁰Núcleo de Astronomía de la Facultad de Ingeniería y Ciencias, Universidad Diego Portales, Av. Ejército Libertador 441, Santiago, Chile

³¹Las Campanas Observatory, Carnegie Institution of Washington, Casilla 601, La Serena, Chile

³²Space Telescope Science Institute, 3700 San Martin Dr., Baltimore, MD 21218, USA

³³ *Department of Space, Earth and Environment, Chalmers University of Technology, Onsala Space Observatory, SE-43992 Onsala, Sweden*

³⁴ *DTU-Space, Technical University of Denmark, Elektrovej 327, DK2800 Kgs. Lyngby, Denmark*

³⁵ *Cosmic Dawn Center (DAWN), Jagtvej 128, DK2200 Copenhagen N, Denmark*

³⁶ *DTU-Space, Technical University of Denmark, Elektrovej 327, 2800, Kgs. Lyngby, Denmark*

³⁷ *Niels Bohr Institute, University of Copenhagen, Jagtvej 128, 2200, Copenhagen N, Denmark*

³⁸ *Univ Lyon, Univ Lyon1, Ens de Lyon, CNRS, Centre de Recherche Astrophysique de Lyon UMR5574, F-69230, Saint-Genis-Laval, France*

³⁹ *Waseda Research Institute for Science and Engineering, Faculty of Science and Engineering, Waseda University, 3-4-1 Okubo, Shinjuku, Tokyo 169-8555, Japan*

⁴⁰ *National Astronomical Observatory of Japan, 2-21-1, Osawa, Mitaka, Tokyo, Japan*

⁴¹ *Division of Particle and Astrophysical Science, Graduate School of Science, Nagoya University, Nagoya 464-8602, Japan*

⁴² *Institute for Advanced Research, Nagoya University, Furocho, Chikusa, Nagoya 464-8602, Japan*

⁴³ *Department of physics, Graduate School of Science, Nagoya University, Nagoya, Aichi 464-8602, Japan*

⁴⁴ *IPAC, California Institute of Technology, Mail Code 314-6, 1200 E. California Blvd., Pasadena, CA 91125*

(Received December 15, 2022; Revised December 13, 2023; Accepted January 26, 2024)

ABSTRACT

We present ALMA deep spectroscopy for a lensed galaxy at $z_{\text{spec}} = 8.496$ with $\log(M_{\text{star}}/M_{\odot}) \sim 7.8$ whose optical nebular lines and stellar continuum are detected by *JWST*/NIRSpec and NIRCам Early Release Observations in SMACS0723. Our ALMA spectrum shows [O III]88 μm and [C II]158 μm line detections at 4.0σ and 4.5σ , respectively. The redshift and position of the [O III] line coincide with those of the *JWST* source, while the [C II] line is blue-shifted by 90 km s^{-1} with a spatial offset of $0''.5$ ($\approx 0.5 \text{ kpc}$ in source plane) from the centroid of the *JWST* source. The NIRCам F444W image, including [O III] λ 5007 and $\text{H}\beta$ line emission, spatially extends beyond the stellar components by a factor of > 8 . This indicates that the $z = 8.5$ galaxy has already experienced strong outflows as traced by extended [O III] λ 5007 and offset [C II] emission, which would promote ionizing photon escape and facilitate reionization. With careful slit-loss corrections and removals of emission spatially outside the galaxy, we evaluate the [O III]88 μm / λ 5007 line ratio, and derive the electron density n_e by photoionization modeling to be $220_{-130}^{+230} \text{ cm}^{-3}$, which is comparable with those of $z \sim 2-3$ galaxies. We estimate an [O III]88 μm /[C II]158 μm line ratio in the galaxy of > 4 , as high as those of known $z \sim 6-9$ galaxies. This high [O III]88 μm /[C II]158 μm line ratio is generally explained by the high n_e as well as the low metallicity ($Z_{\text{gas}}/Z_{\odot} = 0.04_{-0.02}^{+0.02}$), high ionization parameter ($\log U > -2.27$), and low carbon-to-oxygen abundance ratio ($\log(\text{C}/\text{O}) = [-0.52 : -0.24]$) obtained from the *JWST*/NIRSpec data; further [C II] follow-up observations will constrain the covering fraction of photodissociation regions.

Keywords: galaxies: formation — galaxies: evolution — galaxies: high-redshift

1. INTRODUCTION

Studying early systems in the Epoch of Reionization (EoR; $z \gtrsim 6$) is key to understanding fundamental cosmological questions such as the development of large-scale structure, the processes of cosmic reionization, and the first galaxy formation in the universe. In the last decades, deep *Hubble Space Telescope* (*HST*) surveys provided thousands of EoR galaxies and initial characterization of their stellar component, in terms of unobscured star formation and sizes in the rest-frame ultra-

violet (UV) wavelengths (e.g., Ellis et al. 2013; Bouwens et al. 2015; Finkelstein et al. 2015; Oesch et al. 2016).

The Atacama Large Millimeter/submillimeter Array (ALMA) offers a unique rest-frame far-infrared (FIR) window on EoR galaxies to characterize the dust and gas properties of their interstellar media (ISMs), where the major cooling lines (e.g., [C II] 158 μm , [O III] 88 μm) and underlying dust continuum are probes of key mechanisms in the ISM such as disk rotation (e.g., Smit et al. 2018; Rizzo et al. 2020), gravitational instability (e.g., Tadaki et al. 2018), formation of the bulge, disk, and spiral arms (e.g., Tsukui & Iguchi 2021; Lelli et al. 2021), galaxy mergers (e.g., Le Fèvre et al. 2020), outflows (e.g., Spilker et al. 2018), and dust-obscured star-forming activities (e.g., Bowler et al. 2022; Inami et al.

* Hubble Fellow

2022), which strongly complements rest-UV studies with *HST*. Since elements produced in stars are returned to the ISM, the metal gas properties traced by the fine-structure lines, with their different ionization potentials and critical densities, provide powerful probes on the star-formation history and related physical conditions of the ISM, such as the temperature, density, ionization, and metal enrichment (e.g., Maiolino & Mannucci 2019).

Previous ALMA observations have also raised questions about what causes large diversity in EoR galaxies and the difference from local galaxies. Early deep ALMA [C II] spectroscopy of some EoR galaxies has shown low $L_{[\text{C II}]}/\text{SFR}$ values (e.g., Ota et al. 2014; Knudsen et al. 2016), suggesting that they have characteristic ISM conditions such as high ionization parameter, low metallicity, or low gas density (e.g., Ferrara et al. 2019). However, recent ALMA observations detected dust continuum (e.g., Watson et al. 2015; Inami et al. 2022) and bright [C II] lines (e.g., Bouwens et al. 2022), pointing to a $L_{[\text{C II}]}/\text{SFR}$ relation similar to that of local main-sequence galaxies (e.g., Schaerer et al. 2020) and even low-mass sub- L^* galaxies at $z \gtrsim 6$ (e.g., Fujimoto et al. 2021; Molyneux et al. 2022). Moreover, while ALMA observations of EoR galaxies have also shown high $L_{[\text{O III}]} / L_{[\text{C II}]}$ ratios (e.g., Inoue et al. 2016; Harikane et al. 2020; Carniani et al. 2020; Witstok et al. 2022) that are comparable or even higher than local dwarf galaxies (e.g., Cormier et al. 2015), the main driver for the high ratios is still under debate (e.g., Harikane et al. 2020; Vallini et al. 2021; Katz et al. 2022; Witstok et al. 2022). While promising, past *HST* and ALMA results have yet to provide a clear picture of the ISM physics in EoR galaxies.

To understand ISM physics, one of the key quantities is the gas-phase metallicity (Z_{gas}), which is a direct probe of chemical enrichment and, thus, the evolutionary stage of galaxies. The flux of each metal line is determined by the abundance of that element and its emissivity (Aller 1984). Therefore, we can accurately estimate the abundance once we measure the emissivity based on the electron temperature T_e , i.e., the so-called *direct method* (e.g., Pilyugin & Thuan 2005; Andrews & Martini 2013). However, since the direct method requires the detection of very faint auroral lines (e.g., [O III] $\lambda 4363$), this has until recently only been possible for a handful of sources up to $z \sim 3$ (e.g., Christensen et al. 2012; Kojima et al. 2017; Sanders et al. 2020).

Our observational landscape has been revolutionized by the advent of *JWST*. As part of the Early Release observation (ERO) programs of *JWST*, deep NIRSpec multi shutter array (MSA) observations have

been performed towards the massive lensing cluster SMACSJ0723, successfully detecting multiple nebular emission lines in the rest-frame UV to optical wavelengths and determining spectroscopic redshifts for distant lensed galaxies out to $z = 8.496$ (e.g., Carnall et al. 2023; Schaerer et al. 2022; Trump et al. 2022; Curti et al. 2022). Remarkably, the deep NIRSpec spectra also show the detection of the auroral line [O III] $\lambda 4363$, enabling the first direct temperature T_e method estimates at such high redshifts (e.g., Schaerer et al. 2022; Trump et al. 2022; Curti et al. 2022). With the powerful *JWST* and ALMA combination, we are finally in a position to fully reveal how the elements of galaxies – gas, stellar, and dust – interplay with each other and what governs the growth of galaxies in the infant Universe.

In this paper, we present ALMA deep follow-up of two major coolant lines, [C II] $158\mu\text{m}$ and [O III] $88\mu\text{m}$, and underlying continuum for the lensed galaxy at $z = 8.496$, whose warm ISM properties are best characterized by the latest deep *JWST* observations, including the [O III] $\lambda 4363$ line. This is the first FIR characterization of an EoR galaxy with a robust metallicity measurement via the *direct method*, setting the benchmark to understand and interpret previous results from ALMA EoR galaxy studies over the last decade and providing a timely, unique reference for future follow-up of EoR galaxies in the coming decade.

The structure of this paper is as follows. In Section 2, we describe the observations and the data processing of both *JWST* and ALMA. Section 3 outlines the analyses related to the mass model for the lensing cluster, measurements of flux, size, and morphology, and the optical–mm SED fitting. In Section 4, we present the results from the multiple-line studies and discuss the physical origins of these results. A summary of this study is presented in Section 5. Throughout this paper, we assume a flat universe with $\Omega_m = 0.3$, $\Omega_\Lambda = 0.7$, $H_0 = 70 \text{ km s}^{-1} \text{ Mpc}^{-1}$, and the Chabrier initial mass function (IMF; Chabrier 2003). We adopt an angular scale of $1'' = 4.63 \text{ kpc}$ for the target redshift at $z = 8.496$. We take the cosmic microwave background (CMB) effect into account and correct the flux measurements at submm and mm bands, following the recipe presented by da Cunha et al. (2013) (see also e.g., Pallottini et al. 2015; Zhang et al. 2016; Lagache et al. 2018).

2. OBSERVATIONS & DATA PROCESSING

2.1. SMACS J0723.3-7327

The target field, SMACS J0723.3-7327 (hereafter SM0723), is a massive galaxy cluster at $z = 0.390$ ($07^h 23^m 13.3^s$, $-73^d 27^m 25^s$), initially discovered via the Sunyaev-Zel’dovich effect in the Planck survey (Planck

Table 1. ALMA DDT Observation & Data Properties for ID4590 at $z = 8.496$ in SM0723

Target line	Band	λ_{cent} (μm)	Obs Date (YYYY-MM-DD)	Baseline (m)	N_{ant}	T_{int} (min)	PWV (mm)	beam ($'' \times ''$)	σ_{line} ($\mu\text{Jy}/\text{beam}$)	σ_{cont} ($\mu\text{Jy}/\text{beam}$)
(1)	(2)	(3)	(4)	(5)	(6)	(7)	(8)	(9)	(10)	(11)
[C II] 158 μm	5	1540	2022-10-17	15.1–629.3 (C3)	44	85.7	0.5	1.35×1.25	225	11.6
[O III] 88 μm	7	854	2022-10-14	15.1–629.3 (C3)	44	99.8	0.4	0.71×0.58	420	20.9

NOTE— (1) FIR fine-structure atomic cooling line targeted in this program. (2) ALMA Band. (3) Central wavelength corresponding to the central sky frequency in the observation. (4) Observation date. (5) Baseline range. The parenthesis shows the configuration. (6) Number of antennae. (7) On-source integration time in minutes. (8) Mean precipitable water vapor (PWV) during the observations. (9) Synthesized beam size (FWHM) in the natural-weighted image. (10–11) Standard deviation of the pixels. For the cube, we show the value in the channel corresponding to the line frequency in the 20-km s^{-1} data cube.

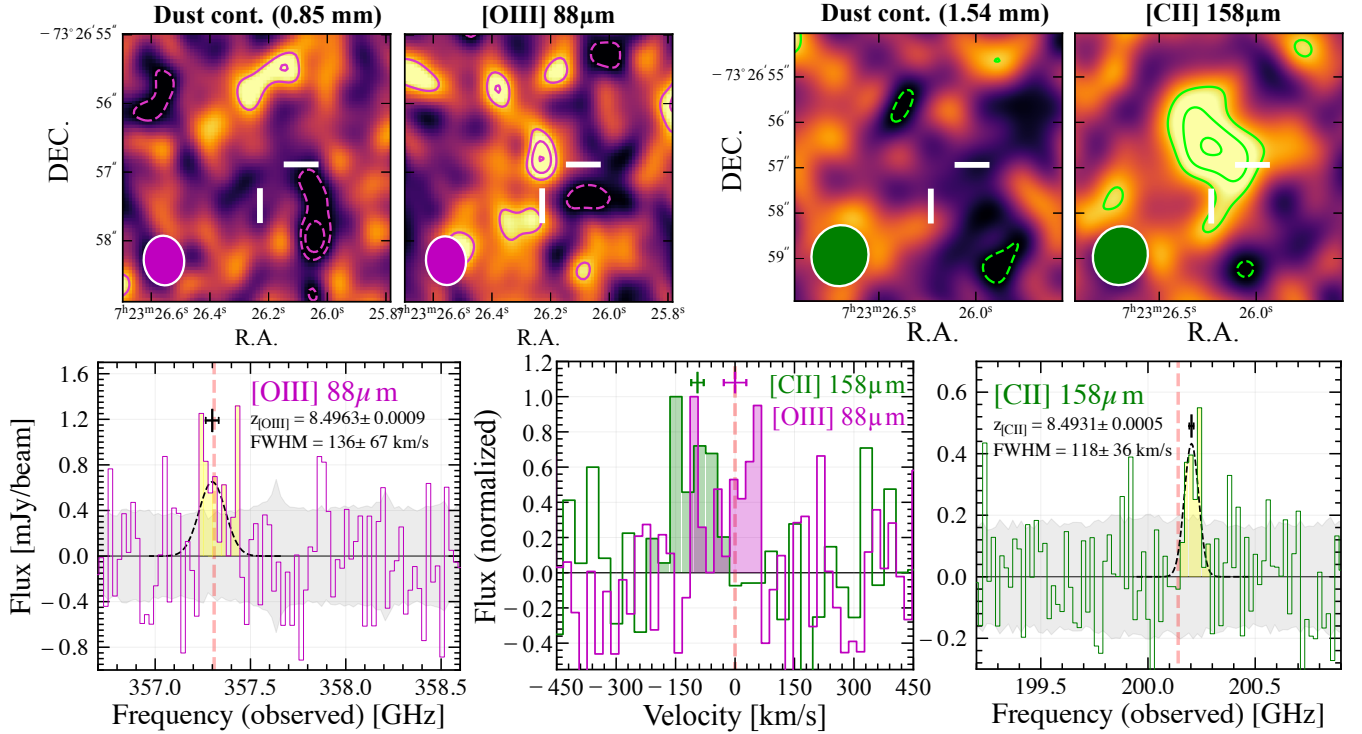


Figure 1. Summary of ALMA DDT observation results. **Top:** The ALMA dust continuum and velocity-integrated line maps for the [O III]88 μm ($4'' \times 4''$) and [C II]158 μm lines ($6'' \times 6''$). The solid (dashed) contours are the 2σ , 3σ , and 4σ (-3σ and -2σ) levels. The white bars indicate the target position at the center of the maps, and the ellipse denotes the synthesized ALMA beam. **Bottom:** ALMA line spectra, where the middle panel compares their line profiles in the velocity frame, where the zero velocity is based on $z = 8.496$ determined by NIRSspec. The spectra are extracted from the mean pixel count within optimized apertures smaller than the beam size at the source position. The dashed curve shows the best-fit Gaussian. The black bar shows the best-fit frequency center of the line with the 1σ error, and the corresponding redshift and the line width are described in the label. The grey shade denotes the 1σ error in each channel. The red dashed vertical line denotes the expected line frequency based on the redshift of $z = 8.496$ determined by NIRSspec.

Collaboration et al. 2011). The galaxy cluster mass is estimated to be $M_{200} = 8.4 \times 10^{14} M_{\odot}$. SM0723 was observed as part of the *HST* Reionization Lensing Cluster Survey (RELICS, #GO-14096, PI: D. Coe, Coe et al. 2019) treasury program and the subsequent *Spitzer* S-RELICS program (#12005, PI: M. Bradac).

2.2. ALMA

ALMA Band 5 and Band 7 follow-up observations of [C II] and [O III] spectroscopy were carried out on October 17th and 14th 2022, respectively, as a Cycle 8 DDT program (#2022.A.00022.S, PI: S. Fujimoto). The target was a strongly lensed star-forming galaxy, ID4590, spectroscopically confirmed at $z = 8.496$ with the robust detection of rest-frame optical emission lines including the [O III] λ 4363 line (e.g., Carnall et al. 2023; Schaerer et al. 2022; Trump et al. 2022; Curti et al. 2022). Both observations used the Frequency Division Mode, and baseline ranges 15–457 m in the C-3 configuration. The mean precipitable water vapour (PWV) was 0.5 mm and 0.4 mm, and the on-source integration times were 85.7 mins and 99.8 mins in Band 5 and Band 7, respectively. J0519-4546 was observed as a flux and bandpass calibrator in both observations, while the phase calibration was performed with J0601-7036 and J0635-7516 in Band 5 and Band 7 observations, respectively.

The ALMA data were reduced and calibrated with the Common Astronomy Software Applications package version 6.4.1.12 (CASA; THE CASA TEAM et al. 2022) with the pipeline script in the standard manner. We imaged the calibrated visibilities using natural weighting, a pixel scale of $0''.05$, and a primary beam limit down to 0.2 by running the CASA task TCLEAN. For cubes, we adopted spectral channel bins of 20, 30, and 40 km s^{-1} and performed the CLEAN algorithm. We confirmed the results unchanged much ($<10\%$) in the following analyses via the choice of the spectral resolutions, and we used 20 km/s resolution cubes in the following analyses. For continuum maps, the TCLEAN routines were executed down to the 1σ level with a maximum iteration number of 100,000 in the automask mode (Kepley et al. 2020). We mask the central $\pm 120 \text{ km s}^{-1}$ channels to avoid contamination from the [C II] and [O III] lines in the continuum map. The natural weighted images, which maximize the S/N, resulted in the full-width-half-maximum (FWHM) size of the synthesized beam of $1''.35 \times 1''.25$ and $0''.71 \times 0''.58$ with 1σ sensitivities for the continuum (line in a 20 km s^{-1} channel) of 11.6 (225) $\mu\text{Jy beam}^{-1}$ and 20.9 (420) $\mu\text{Jy beam}^{-1}$ in Band 5 and Band 7, respectively. Figure 1 shows the reduced continuum maps and the line cubes for both ALMA Band 5

and Band 7. We summarize the data properties of the continuum maps and the line cubes in Table 1.

2.3. JWST

As part of the *JWST* ERO (#ERO-2736; Pontoppidan et al. 2022), SM0723 was observed with *JWST*/NIRCam, NIRSpec, MIRI, and NIRISS in June 2022. In the NIRCam and MIRI observations, six (F090W, F150W, F200W, F277W, F356W, F444W) and four (F770W, F1000W, F1500W, F1800W) different filters were used with ~ 7540 sec and ~ 5600 sec exposure per filter, reaching 5σ limiting magnitudes of ~ 29.4 – 30.0 AB and ~ 23 – 26.3 AB, respectively (Pontoppidan et al. 2022).

For NIRCam and MIRI, we use publicly available reduced and calibrated imaging products via the `grizli` pipeline.¹ The detailed calibration and reduction procedures will be presented in Brammer et al. (in prep.) (see also, e.g., Bradley et al. 2022; Fujimoto et al. 2023). Briefly, the *JWST* pipeline calibrated level-2 NIRCam imaging products were retrieved and processed with the `grizli` pipeline (Brammer & Matharu 2021; Brammer 2023), where the photometric zero-point correction was applied, including other corrections for “snowballs”², “wisps”³, and detector variations.⁴ We include a systematic error of 10% on the observed flux values in the following analyses as a conservative measure in the same manner as other recent NIRCam studies (e.g., Naidu et al. 2022; Finkelstein et al. 2023), while the derived photometric zeropoints are consistent with those derived by other teams for *JWST* ERS programs (Boyer et al. 2022; Nardiello et al. 2022). The fully-calibrated images in each filter were aligned with the GAIA DR3 catalog (Gaia Collaboration et al. 2021), co-added, and drizzled at a 20 mas and 40 mas pixel scale for the short-wavelength (SW: F090W, F150W, F200W) and long-wavelength (LW: F277W, F356W, F444W) NIRCam band images, respectively. For the produced maps, we also additionally correct the proper motion effects of the GAIA sources. In the Appendix, we show the residual astrometric offsets of the GAIA sources. We confirm the residual astrometric offset with respect to the GAIA DR3 frame is close to zero with the uncertainty of ~ 10 – 20 mas. All the MIRI images (F770W, F1000W, F1500W, F1800W) are aligned, co-added, and

¹ <https://s3.amazonaws.com/grizli-v2/JwstMosaics/v4/index.html>

² <https://jwst-docs.stsci.edu/data-artifacts-and-features/snowballs-artifact>

³ <https://jwst-docs.stsci.edu/jwst-near-infrared-camera/nircam-features-and-caveats/nircam-claws-and-wisps>

⁴ <https://github.com/gbrammer/grizli/pull/107>

drizzled at 40 mas pixel scale in the same manner. Existing multi-wavelength WFC3 archival imaging from *HST* was also processed with `grizli`, being aligned, co-added, and drizzled at 40 mas pixel scale in the same manner (see also Kokorev et al. 2022). We include all MIRI and *HST*/F105W, F125W, F140W, and F160W data in our analysis. Given the existence of nearby objects (Section 3.4), we adopt $0''.36$ -diameter aperture photometry which is corrected to the total flux measurement by `MAG_AUTO`. We also correct for the Galactic dust reddening in the target direction. The *JWST* and *HST* photometry used in this paper are summarized in the Appendix.

For NIRSspec, there are several studies applying the latest reduction and calibration (Heintz et al. 2023; Nakajima et al. 2023), compared to previous studies (e.g., Schaerer et al. 2022; Curti et al. 2022; Trump et al. 2022; Brinchmann 2022; Arellano-Córdova et al. 2022). In our paper, we use results from Nakajima et al. (2023) due to requirements of specific parameter sets for the photoionization model analysis in Section 4.5 that are self-consistently derived in Nakajima et al. (2023). We confirm that the measurements and the derived physical parameters are generally consistent with the previous studies within the errors (e.g., Schaerer et al. 2022; Curti et al. 2022; Trump et al. 2022; Brinchmann 2022; Arellano-Córdova et al. 2022) as well as the similarly latest calibration and reduction efforts presented in Heintz et al. (2023). Briefly, the NIRSspec 1D spectra are re-created by using four of the six exposures after removing one with no signal and another with a noisy 2D spectrum around $H\gamma + [\text{O III}]\lambda 4363$. Some improvements are also implemented, including the background residual subtractions, hot pixel removals, optimal 1D extractions, as well as flux calibrations by referring to the standard star observations taken during commissioning. Using the improved NIRSspec spectrum, Nakajima et al. confirm the rest-frame UV and optical emission line detection at $z = 8.496$ from ID4590, including $[\text{O III}]\lambda 5007, 4959, [\text{O III}]\lambda 4363, H\beta, H\gamma, H\delta$, and $\text{C III}] \lambda \lambda 1907, 1909$, and evaluate their relative line fluxes after applying a slit-loss correction⁵. On the other hand, Nakajima et al. find that the $[\text{O II}]\lambda 3727$ doublet is not clearly detected in every nod and visit, and they place a conservative 3σ upper limit, which provides a lower limit for the ionization parameter $\log(U) > -2.27$ based

⁵ The slit-loss is corrected by convolving and integrating the 1D spectrum with the filter response of F444W to match it with the total magnitude of the NIRCcam photometry, which is derived with a $0''.3$ -diameter circular aperture and the corresponding aperture correction.

Table 2. Observed FIR properties of ID4590 with ALMA

Target line	$[\text{O III}]\lambda 88\mu\text{m}$	$[\text{C II}]\lambda 158\mu\text{m}$
R.A.	07:23:26.242	07:23:26.243
Dec.	-73:26:56.824	-73:26:56.514
S/N _{line}	4.0	4.5
Frequency center [GHz]	357.305 ± 0.034	200.203 ± 0.010
z_{line}	8.4963 ± 0.0009	8.4931 ± 0.0005
Line width [km s^{-1}]	136 ± 67	118 ± 36
Line intensity [Jy km s^{-1}]	$0.113 \pm 0.033^\ddagger$	$0.094 \pm 0.027^\ddagger$
Line luminosity [$\times 10^8 L_\odot$]	$3.12 \pm 0.89^\ddagger$	$1.45 \pm 0.32^\ddagger$
Continuum [μJy]	$< 41.8 (0.85 \text{ mm}) < 23.2 (1.54 \text{ mm})$	

[‡] We add a possible uncertainty by 20% due to the velocity-integration range for the $[\text{O III}]$ line (see text).

[†] Given the spatial and velocity offsets of the $[\text{C II}]$ line, we place a 3σ upper limit of $L_{[\text{C II}]} < 6.0 \times 10^7 L_\odot$ at the galaxy position from the residual map of IMFIT.

on Kewley & Dopita (2002). The electron temperature and the gas-phase oxygen abundance are estimated to be $T_{[\text{O III}]} = (2.08 \pm 0.34) \times 10^4 \text{ K}$ and $12 + \log(\text{O}/\text{H}) = 7.26 \pm 0.18$ (equal to $0.04 \pm 0.02 Z_\odot$ by assuming the solar metallicity of $12 + \log(\text{O}/\text{H}) = 8.69$) via the direct T_e method (e.g., Pilyugin et al. 2012) by assuming a negligible contribution from O^+/H^+ (< 0.05 dex at 3σ ; Nakajima et al. 2023). The lower and upper boundaries of the C/O abundance are also estimated to be $\log(\text{C}/\text{O}) = [-0.52 : -0.24]$ (Isobe et al. 2023b). These physical parameters are derived including the dust correction based on the best-fit $E(B-V)$ value in this paper (Section 3.6).

3. DATA ANALYSIS

3.1. Mass Model

Several mass models are publicly available in SM0723, including those developed by using LENSTOOL (Jullo et al. 2007) and GLAFIC (Oguri 2010) with the *HST* data from the RELICS team (Coe et al. 2019)⁶. More models have been constructed for SM0723 with the *JWST* ERO data, using LENSTOOL (Mahler et al. 2022; Caminha et al. 2022), the light-traces-mass approach (LTM; Broadhurst et al. 2005; Zitrin et al. 2009, 2015) presented in Pascale et al. (2022), and an updated version of GLAFIC (Oguri 2021) presented in Harikane et al. (2022).

In this paper, we use the latest GLAFIC model. The magnification factor for ID4590 is estimated to be $\mu =$

⁶ <https://archive.stsci.edu/prepds/relics/>

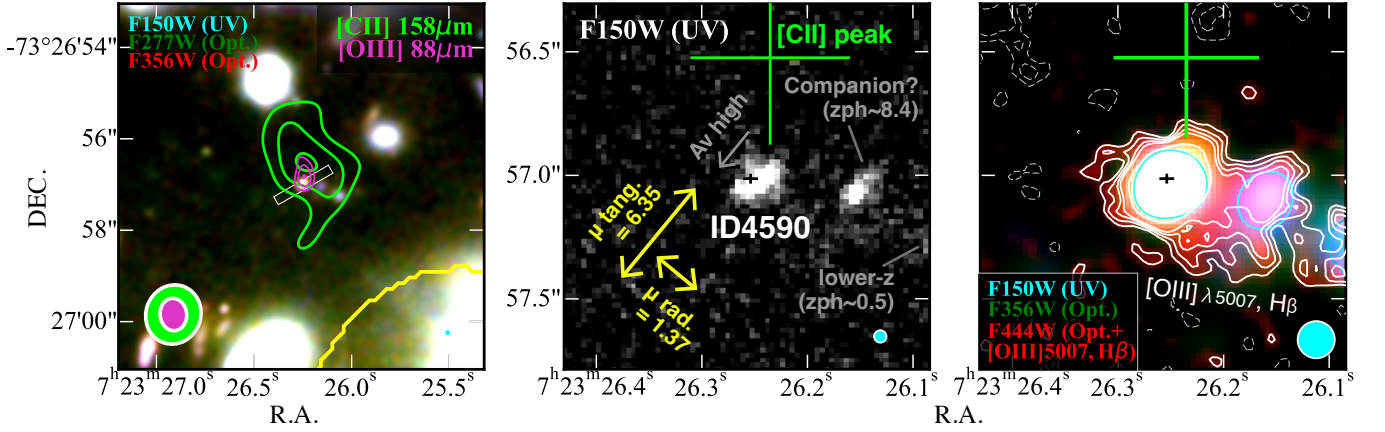


Figure 2. NIRCcam image cutouts around ID4590. **Left:** PSF-matched RGB image ($6'' \times 6''$) whose color assignment is shown in the label. The light green and magenta contours indicate the [C II]158 μm and [O III]88 μm line intensities at 2σ , 3σ , and 4σ levels, respectively. The yellow curve denotes the critical curve at $z = 8.5$ of SMACS0723 taken from the latest GLAFIC model (Section 3.1). The light green and magenta ellipses at the bottom left are the ALMA synthesized beams in Band 5 (for [C II]) and Band 7 (for [O III]). The white rectangle shows the NIRSpect/MSA slit. **Middle:** Zoom-in ($1.5'' \times 1.5''$) NIRCcam/F150W image. The green and black crosses indicate the [C II]158 μm and F444W emission peak positions, where the bar scales correspond to their positional accuracy. The yellow arrows indicate the radial ($\mu_{\text{rad.}}$) and tangential ($\mu_{\text{tang.}}$) magnification factors, which combine for a total magnification of 8.69. There are two nearby ($\sim 0.4''$ – $0.8''$) objects towards the East. The SED fitting with EAZY suggests that the closer one could be a companion of ID4590 with $z_{\text{phot}} \sim 8.4$, while the other is estimated to lie at $z_{\text{phot}} \sim 0.5$. The grey arrow indicates the dust attenuation gradient measured by a pixel-based SED analysis (Giménez-Arteaga et al. 2023), implying that the offset of the [C II] emission is not caused by a dust-obscured star-forming region. **Right:** Zoom-in ($1.5'' \times 1.5''$) PSF-matched RGB image whose color assignment is shown in the label. The white contours indicate the flux distribution in the F444W filter at $\pm 2\sigma$, $\pm 3\sigma$, $\pm 4\sigma$, $\pm 5\sigma$, and $\pm 10\sigma$ levels. For comparison, the cyan contour represents the PSF-matched F150W flux distribution whose intensity relative to the peak is equal to that of the 2σ -level contour in the F444W filter. The F444W filter includes the rest-frame optical continuum and [O III]5007 and H β emission line from ID4590, showing an extended structure more than other NIRCcam filters. The NIRCcam filters are PSF-matched to the F444W filter in the left and right panels.

8.69, which is consistent with the latest LENSTOOL model prediction ($\mu \sim 9$) based on the *JWST* ERO and the latest MUSE data (Caminha et al. 2022). We define the systematic uncertainty due to the choice of the mass model by

$$\Delta\mu \equiv \frac{|\mu_{\text{glafic}} - \mu_{\text{other}}|}{\mu_{\text{glafic}}}, \quad (1)$$

where μ_{glafic} and μ_{other} indicate the magnification factor evaluated by the updated version of GLAFIC and other models, respectively. Among the mass models constructed with the *JWST* ERO data, the $\Delta\mu$ value is estimated to be ~ 15 – 30% for ID4590. In the following analyses when we correct for the gravitationally lensing effect on ID4590, we use $\mu = 8.69$ and add a systematic uncertainty from the mass models of 30%. When correcting physical values for lensing, we do not account for differential magnification in the following analysis, as we confirm it to be much less than the above systematic uncertainty across the positions in the galaxy. However, when we discuss the intrinsic morphology and size (Section 3.3 and 3.4), we do consider the difference between the radial ($\mu_{\text{rad.}}$) and tangential ($\mu_{\text{tang.}}$) magnifications

that are estimated to be $\mu_{\text{rad.}} = 1.37$ and $\mu_{\text{tang.}} = 6.35$ with position angle (PA) in East of North of -39.5 deg.

3.2. Continuum & Line Measurements

In the top panels of Figure 1, we show the $6'' \times 6''$ continuum maps of ALMA Band 7 (left) and Band 5 (right). In both bands, we find that the relevant pixels show negative counts. We assume that the emission is unresolved in the continuum maps with the current ALMA beam ($\sim 0.7''$ – $1.3''$) and place 2σ upper limits of $41.8 \mu\text{Jy beam}^{-1}$ and $23.2 \mu\text{Jy beam}^{-1}$ in Band 7 and Band 5, respectively, based on the standard deviation of the maps.

In the bottom panels of Figure 1, we also present the line spectra for the [O III]88 μm (left) and [C II]158 μm lines (right). In the spectra, we identify positive signals in several consecutive channels at around 357.3 GHz and 200.2 GHz in Band 7 and Band 5, respectively, that are both consistent with the expected frequencies of the [O III]88 μm and [C II]158 μm lines based on the source redshift spectroscopically determined by NIRSpect. In the top panels, we show the velocity-integrated (moment 0) maps by using these line-detected channels that are

highlighted by the yellow shades in the bottom spectra. In the moment 0 maps, we find that the S/N in the peak pixel shows 4.0 and 4.1 for the [O III] and [C II] lines, respectively. The latter is spatially resolved, especially in the Northwest to Southeast direction, where the S/N increases to 4.5 with a 2''-diameter aperture. On the other hand, [O III] line is compact and not spatially resolved with the current beam size and data depth. Note that the [O III] line shows a potential double peak profile, which is typical among rotation-supported systems with inclinations (e.g., Kohandel et al. 2019), while the other possibility is that the noise fluctuation skews the line profile from a single Gaussian. We confirm that removing the three channels around the secondary peak ($\simeq 357.45$ GHz) from the integration range for the mom 0 map provides the same peak S/N of 4.0. This suggests that the significance level of the [O III] line detection is not unchanged regardless of whether it is truly the double peak profile or not.

From a single Gaussian fit in the spectra, we estimate the frequency center and the line redshifts as $z_{[\text{O III}]88} = 8.4963 \pm 0.0009$ and $z_{[\text{C II}]} = 8.4931 \pm 0.0005$ with the line width of $\text{FWHM}_{[\text{O III}]88} = 137 \pm 67 \text{ km s}^{-1}$ and $\text{FWHM}_{[\text{C II}]} = 118 \pm 36 \text{ km s}^{-1}$. The redshift of [O III]88 μm is in excellent agreement with the source redshift determined by NIRSpec, while the [C II] line appears blue-shifted by $\sim 90 \text{ km s}^{-1}$ beyond the errors. The line widths are consistent with each other within the errors.

Given a possibility that the chance projection of the noise fluctuation (e.g., Kaasinen et al. 2022) causes the [C II] velocity offset, we quantify its probability in our [C II] line identification by running a blind line search algorithm of FINDCLUMP implemented in a Python library of INTERFEROPY (Boogaard et al. 2021a) for observational radio-mm interferometry data analysis⁷. We use a 20-km⁻¹ channel width cube of Band 5 and adopt the spatial tolerance of 1''2 (= beam size) and the frequency tolerance of 100 MHz ($\sim 150 \text{ km s}^{-1}$) to match the detection in the cube. We find that ~ 180 line features are identified with similar or higher S/N in the entire data cube within a 20''-radius circular area and 274 channels, which is equal to 259793 independent beams in the cube. Given that the 200.2 GHz line is identified within the spatial and frequency tolerances from the expectations of the target, we estimate the chance projection of the random noise is 0.07% ($= 180 / 259793 \times 1$), indicating that the purity of the line detection is $> 99.9\%$. Therefore, we conclude that [C II] line identifi-

cation is unlikely explained by the noise fluctuation, and its velocity and spatial offsets are real. The reason for the blue-shifted [C II] would be differential distributions of the multi-phase gases and their associated kinematics (e.g., Pallottini et al. 2019; Arata et al. 2020; Kohandel et al. 2020; Katz et al. 2022; Akins et al. 2022; Valentino et al. 2022); the rest-frame optical emission lines observed with NIRSpec and the [O III]88 μm line originate from the ionized gas, while the [C II]158 μm line mostly arises in the photodissociation regions (PDRs). The [C II] peak position shows a spatial offset from the *JWST* source position by $\sim 0''.5$ beyond the uncertainty of its positional accuracy (Section 3.4), which also supports the differential distributions of these multi-phase gases.

With a 2''-diameter aperture in the moment 0 maps, we measure the line intensities and convert them to the [C II] line luminosity of $L_{[\text{C II}]} = (1.45 \pm 0.32) \times 10^8 L_{\odot}$ in the observed frame (i.e., no lens correction). Given its spatial and velocity offsets, we also place a 3σ upper limit at the galaxy position of $< 6.0 \times 10^7 L_{\odot}$ by taking the line width from [O III] line. From its compact morphology of [O III] 88 μm , we assume that [O III] is spatially unresolved and infer the [O III] line luminosity of $L_{[\text{O III}]} = (3.12 \pm 0.76) \times 10^8 L_{\odot}$ from the peak pixel count. Note that this [O III] line flux estimate decreases by $\sim 20\%$ if we remove the three channels around the secondary peak from the integration range when generating the moment 0 map. We thus add a systematic uncertainty of 20% for the [O III] line flux estimate in the following analyses. We summarize these continuum and line properties in Table 2.

3.3. Sizes

We also measure the spatial sizes of [C II]158 μm and [O III]88 μm lines with ALMA as well as the rest-frame UV and optical continuum with *JWST*/NIRCam. In both data, we measure the sizes in the image plane.

First, for the [C II] and [O III] lines, we perform CASA IMFIT task to apply the 2D elliptical Gaussian fitting. We do not fix any parameters in the fitting. We obtain the best-fit FWHM of $1''.90 \pm 0''.82$ and $0''.99 \pm 0''.57$ in the major and minor axis, respectively, for the [C II] line. Although we cannot exclude the possibility that these best-fit sizes are affected by the noise fluctuation with the current S/N, we confirm that no significant positive/negative signals remain in the residual map. On the other hand, the IMFIT output suggests that [O III] is not spatially resolved. We subtract the ALMA synthesized beam profile re-scaled to the [O III] peak count from the observed [O III] map and confirm that no significant positive/negative signals remain in the resid-

⁷ <https://interferopy.readthedocs.io/en/latest/index.html>

ual map. We thus place a 2σ upper limit of FWHM $< 0''.31$ based on the limit of the reliable size measurement with interferometric data according to the data sensitivity and the beam size (Martí-Vidal et al. 2012). The trend of the larger [C II] line size than that of the [O III] line is consistent with recent ALMA observation results for galaxies at similar redshifts (Carniani et al. 2020; Akins et al. 2022; Witstok et al. 2022). We list the circularized effective radii⁸ of the [C II] and [O III] lines in Table 3. The observed, best-fit model and residual maps are summarized in the Appendix.

Second, for the rest-frame UV and optical continuum, we use the NIRCcam/F150W and F356W maps, respectively, that are not affected by strong emission line contributions. We conduct a 2D Sérsic profile fitting with GALFIT (Peng et al. 2010). The pixel of the F356W map is rebinned to a pixel scale of $0''.02$, which is the same pixel scale as the F150W map. We use NIRCcam PSFs for the ERO data of SM0723 publicly available⁹, which are generated from the WebbPSF model and drizzled to a grid of $0''.02$ in the same manner as the mosaic maps in the `grizli` pipeline. Note that these PSFs are generated with the latest version of WebbPSF, including the correction of the optical path difference¹⁰, where it mitigates the potential difference from the empirical PSFs (e.g., Ono et al. 2022). In the F150W fit for the rest-frame UV continuum, we do not fix any parameters, while we adopt the initial parameter set based on the lensing distortion with the axis ratio of $\mu_{\text{rad.}}/\mu_{\text{tang.}} = 0.22$ and the PA of -39.5 deg. We obtain the best-fit effective radius of $r_e = 3.6 \pm 0.5$ pixel ($= 0.33 \pm 0.05$ kpc) in the major axis with the axis ratio of 0.57 ± 0.09 . The best-fit axis ratio exceeds the prediction from the lensing distortion ($= 0.22$), indicating that ID4590 is well resolved in the radial magnification axis. We also obtain the PA of -38 ± 10 deg, which is consistent with the lensing distortion ($= -39.5$). This supports the strong magnification factor in ID4590 of 8.69 ($= \mu_{\text{rad.}} \times \mu_{\text{tang.}}$) and suggests that the observed rest-frame UV morphology is mostly dominated by the lensing distortion. In the F356W fit for the rest-frame optical continuum, we fix the best-fit axis ratio, PA, and Sérsic index from the F150W results, given the worse spatial resolution than that of F150W. We obtain the best-fit r_e of 3.9 ± 0.2 pixel ($= 0.36 \pm 0.02$ kpc) in the major axis. Given the best-fit axis ratio of 0.57 ± 0.09 , we list the circularized r_e values for these stellar continua also in Table 3. The observed,

best-fit model, and residual maps for these NIRCcam results are also summarized in the Appendix.

3.4. Morphology

In Figure 2, we compare the spatial distribution of each emission from ID4590. The left panel shows the [C II]158 μm and [O III]88 μm line contours overlaid on the $6'' \times 6''$ RGB color image with NIRCcam filters. The middle and right panels display zoom-in ($1''.5 \times 1''.5$) F150W image (middle) and RGB color image (right) with NIRCcam filters of F150W, F356W, and F444W, where the first two filters trace the rest-frame UV and optical continuum, while the last filter includes the [O III]5007 and H β lines in addition to the underlying rest-frame optical continuum. For the RGB images, the maps are PSF-matched to the F444W filter, and the white and cyan contours in the right panel represent the flux distribution in the F444W and F150W filters, respectively. The green and black crosses indicate the peak position of the [C II]158 μm line and the F444W emission, where the bar sizes of the cross are equal to the uncertainty of the positional accuracy based on its beam size and S/N¹¹. The yellow arrows in the middle panel denote the radial ($\mu_{\text{rad.}}$) and tangential magnifications ($\mu_{\text{tang.}}$) to understand the distortion of ID4590 due to the lensing effect. To investigate faint tails of the emission, we additionally subtract the local background in all NIRCcam filters by evaluating the median pixel count in a black field near from ID4590.

We find that the peak position of the [O III]88 μm is consistent with the *JWST* source position of ID4590, while the [C II]158 μm has an offset of $\sim 0''.5$ beyond the uncertainty of the positional accuracy. In the source-plane reconstruction of the *JWST* and [C II] source positions, we find that the intrinsic offset decreases down to $\sim 0''.1$, which is equal to ~ 0.5 kpc. Because of the significantly low probability of the chance projection of the noise (Section 3.2), the spatial offset in [C II] indicates that physical origins of the emission is associated with ID4590, while it arises outside the galaxy (e.g., Maiolino et al. 2015; Carniani et al. 2017). We further discuss the physical origins of the [C II] offset in Section 4.4.

We also find that the emission in the F444W filter is extended more than the rest-frame UV and optical continuum observed in F150W and F356W filters. We interpret this extended emission attributed to strong

⁸ The effective radius is almost FWHM / 2.0 in Gaussian.

⁹ <https://github.com/gbrammer/grizli-psf-library>

¹⁰ https://webbpsf.readthedocs.io/en/latest/jwst_measured_ops.html

¹¹ The positional accuracy of ALMA (pos_{acc}) can be approximated by the relationship of $\theta_{\text{beam}} / \text{SNR} / 0.9$, where SNR is the signal-to-noise ratio of the image target peak (<https://help.almascience.org/kb/articles/what-is-the-absolute-astrometric-accuracy-of-alma>).

emission lines of [O III]5007 and H β from ID4590, implying that a powerful mechanism of forming the extended ionized gas structure is taking place. Note that there are two nearby objects towards the East with offsets of $\simeq 0''.4$ and $\simeq 0''.8$. We run the SED fitting code **EAZY** (Brammer et al. 2008) for these two nearby objects with the available *JWST*/NIRCam, MIRI, and *HST* photometry in the public **grizli** catalog (Section 2.3) by using the default template set of **tweak_fspqs_QSF_12.v3**. The results suggest the photometric redshifts of $z_{\text{phot}} = 8.45^{+0.29}_{-0.28}$ and $z_{\text{phot}} = 0.37^{+0.11}_{-0.10}$ each from the nearest. Therefore, the nearest object might be a companion galaxy associated with ID4590. However, if the presence of nearby objects is the cause of the extended structure, the same structure should also be observed in the other NIRCam filters, which is not the case. Besides, the structure is also extended towards South \sim Southeast, where no rest-frame UV continuum is identified. Furthermore, the PSF size of the NIRCam/F444W filter is $\sim 0''.15$, where the emission should be individually resolved if the extended ionized gas is caused by individual further faint satellites. We thus conclude that this diffuse, extended structure in the F444W filter is hardly explained either by these two nearby objects or further faint satellites. The structure extends to $\sim 0''.5$ towards the Southeast most. Given the circularized rest-frame optical effective radius of $0''.059 \pm 0''.010$ (Section 3.3), the structure extends out to ~ 8 times more than the stellar distribution of the galaxy. If we take the differential magnification effects into account, the structure is aligned to the radial magnification axis ($\mu_{\text{rad.}} = 1.37$), indicating that the intrinsic physical distance after the lens correction is ~ 1.7 kpc. For the same direction, the rest-frame optical effective radius after the lens correction is estimated to be 0.11 ± 0.03 kpc. These results suggest that the ionized gas distribution over the effective radius of the stellar distribution even increases to a factor of ~ 15 . The relative ratio of > 8 is well beyond the diffused ionized gas (DIG) structure observed among local galaxies ($\sim 10\%$ of the galaxy size; see e.g., Rossa & Dettmar 2003). We further discuss the physical origins of the extended ionized gas in Section 4.4.

By comparing the total flux correction factors in F356W and F444W filters (Section 2.3), we find that the extended component in F444W contributes to the total flux measurement by $\sim 8\%$. In the following analyses

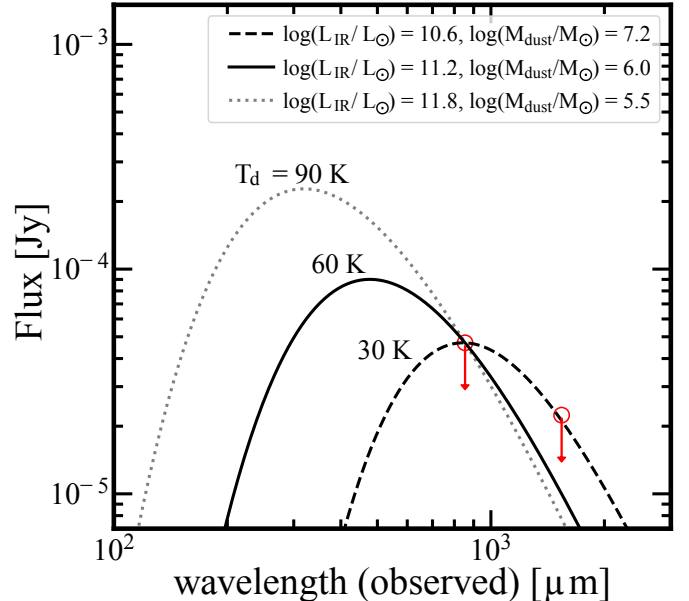


Figure 3. Constrain of the FIR SED of ID4590. The red arrows indicate the 2σ upper limits obtained in ALMA Band 5 and Band 7. The dotted, solid, and dashed curves show the single modified black body (MBB) scaled to the Band 7 upper limit, with the dust temperature of $T_d = 30$ K, 60 K, and 90 K, respectively. In each case, the induced IR luminosity L_{IR} by integrating MBB over 8–1000 μm and the dust mass M_{dust} are shown in the label. We fix the dust spectral index $\beta_d = 1.8$ (e.g., Chapin et al. 2009; Planck Collaboration et al. 2011).

when studying the same emitting regions¹², we remove this 8% contribution of the extended ionized gas to the total flux measurement in the F444W filter. With the same motivation for analyses that assume the emission originated from the same regions, we also use the 3σ upper limit for the [C II] luminosity at the galaxy position IMFIT (Section 3.2).

3.5. FIR SED

From the upper limits of the dust continuum both in Band 5 and Band 7, we attempt to constrain the FIR SED of ID4590. Recent FIR SED studies for high- z dusty star-forming galaxies at $z \sim 1$ –4, including *Herschel* and ALMA photometry, suggest the typical dust temperature of $T_d \sim 30$ K (e.g., Swinbank et al. 2014; Sun et al. 2022). For UV-selected galaxy populations such as Lyman-break galaxies (LBGs) at $z \sim 4$ –7,

¹² We correct the 8% contribution from the extended region in the full SED analysis (Section 3.6). By assuming that [O III]5007 emission also has the same flux contribution from the extended region, we apply the same correction to the [O III]88 μm /[O III]5007 line ratio analysis (Section 4.1).

ALMA multiple band observations show a higher dust temperature distribution typically ranging from ~ 40 K even out to ~ 80 K (e.g., Faisst et al. 2020; Bakx et al. 2020; Akins et al. 2022; Witstok et al. 2022), where several analytical models have been developed and well reproduced the observation results, including the potential redshift evolution of T_d (e.g., Inoue et al. 2020; Fudamoto et al. 2022a; Sommovigo et al. 2022b).

Because of the limited constraints due to lack of the detection in both ALMA Bands, we assume the single modified black body (MBB) for the FIR SED of ID4590. We adopt a fiducial T_d estimate of 60 K based on the extrapolation of the best-fit redshift evolution model of T_d following the decrease of the gas depletion time scale (t_{depl}) derived in Sommovigo et al. (2022b), while we include the uncertainty of T_d by 30 K given the T_d distribution so far observed in high- z LBGs with ALMA. We fix dust spectral index β_d at a typical value of 1.8 (Chapin et al. 2009; Planck Collaboration et al. 2011) and take the CMB temperature effect (e.g., da Cunha et al. 2013) into account in the MBB model.

In Figure 3, we show three MBB models with $T_d = 30$ K, 60 K, and 90 K normalized to the upper limit of Band 7. The inset labels show the derived IR luminosity L_{IR} , integrated over 8–1000 μm , and the dust mass M_{dust} , with the dust opacity coefficient of $\kappa_\nu = 5.1(\nu/\nu_{250\mu\text{m}})^{\beta_d}$. In the observed frame (i.e. no lens correction), we obtain the upper limits of $\log(L_{\text{IR}}/L_\odot) < 11.2$ and $\log(M_{\text{dust}}/M_\odot) < 6.0$ with the fiducial T_d value of 60 K. This indicates that ID4590 has the observed-frame dust-obscured SFR of $\text{SFR}_{\text{IR}} < 16 M_\odot \text{ yr}^{-1}$. The FIR SED properties are summarized in Table 3.

3.6. Full SED analysis and physical properties

Figure 4 shows the *JWST* and ALMA image cutouts, including the segmentation map (top), and the optical–mm photometry in the observed frame (i.e. no lens correction) measured with *HST*, *JWST*, and ALMA for ID4590 (bottom). A significant flux enhancement is observed in the F444W filter (rest-frame $\sim 4000\text{--}5000\text{\AA}$). Some remarkably massive early galaxy candidates have been reported at $z \sim 7\text{--}11$ whose SED shape shows a secondary peak, likely because of the strong Balmer break in the NIRCcam LW filters (Labbe et al. 2022). However, the secondary peak might be explained by contributions from strong emission lines of [O III] $\lambda 5007$ +H β (Endsley et al. 2022), where the lack of the longer wavelength data challenges drawing a definitive conclusion. In contrast, the presence of the MIRI photometry in ID4590 shows the flux enhancement only occurs in the F444W filter, which helps conclude that the flux enhancement in the F444W filter is caused by strong [O III]+H β emission

Table 3. Physical properties of ID4590 in the image plane

Name	ID4590
R.A.	07:23:26.255
Dec.	−73:26:57.041
z_{spec}	8.496
μ^\dagger	8.69
$\text{SFR} \times \mu [M_\odot \text{ yr}^{-1}]$	26_{-4}^{+9}
$M_{\text{star}} \times \mu [10^8 M_\odot]$	$5.3_{-2.6}^{+5.6}$
$L_{\text{UV}} \times \mu [10^{10} L_\odot]$	2.8 ± 0.3
β_{UV}	-1.70 ± 0.07
$E(B - V)$	0.16 ± 0.03
$L_{\text{IR}}^{\dagger\dagger} \times \mu [10^{11} L_\odot]$	< 1.6
$M_{\text{dust}}^{\dagger\dagger} \times \mu [10^6 M_\odot]$	< 1.0
$M_{\text{gas}} \times \mu [10^9 M_\odot]$	7 ± 3^a
$r_{\text{e,UV}}^{\ddagger} \times \sqrt{\mu} [\text{arcsec}]$	0.056 ± 0.012
$r_{\text{e,opt}}^{\ddagger} \times \sqrt{\mu} [\text{arcsec}]$	0.059 ± 0.010
$r_{\text{e,[CII]158}}^{\ddagger} \times \sqrt{\mu} [\text{arcsec}]$	0.69 ± 0.42
$r_{\text{e,[OIII]88}}^{\ddagger} \times \sqrt{\mu} [\text{arcsec}]$	< 0.16
$n_e [\text{cm}^{-3}]$	220_{-130}^{+230}
$T_e [10^4 \text{ K}]$	2.08 ± 0.34^b
$12 + \log(\text{O}/\text{H})$	7.26 ± 0.18^b
$\log(U)$	$> -2.27^b$
$\log(\text{C}/\text{O})$	$[-0.52 : -0.24]^c$

\dagger From the mass model with GLAFIC (Oguri 2010, 2021) using the *JWST* ERO data presented in Harikane et al. (2022). For the lens corrected values, we add a systematic uncertainty of 30% throughout the paper (Section 3.1).

$\dagger\dagger$ Based on the single MBB with $T_d = 60$ K and $\beta_d = 1.8$ without the energy balance, where a T_d difference by ± 30 K changes the estimates by $\sim \pm 0.5\text{--}1.0$ dex (see also Figure 3).

\ddagger Circularized effective radius. The best-fit axis ratio is 0.57 ± 0.09 .

a Heintz et al. (2023)

b Nakajima et al. (2023)

c Isobe et al. (2023b)

lines, rather than a large stellar mass. Such strong contributions of the [O III]+H β lines also agree with the extended morphology observed in the F444W filter, which is interpreted as the presence of the extended ionized gas emission (Section 3.4).

To perform a panchromatic characterization of ID4590, we perform SED fitting to the optical–mm photometry using CIGALE (Burgarella et al. 2005; Noll et al. 2009; Boquien et al. 2019). While we examine the FIR SED in Section 3.5, the SED modelling with CIGALE allows us to take the energy balance between the dust absorption and re-emission into account, which is complementary with the independent FIR SED analysis. The fitting was performed similarly as in Fujimoto et al.

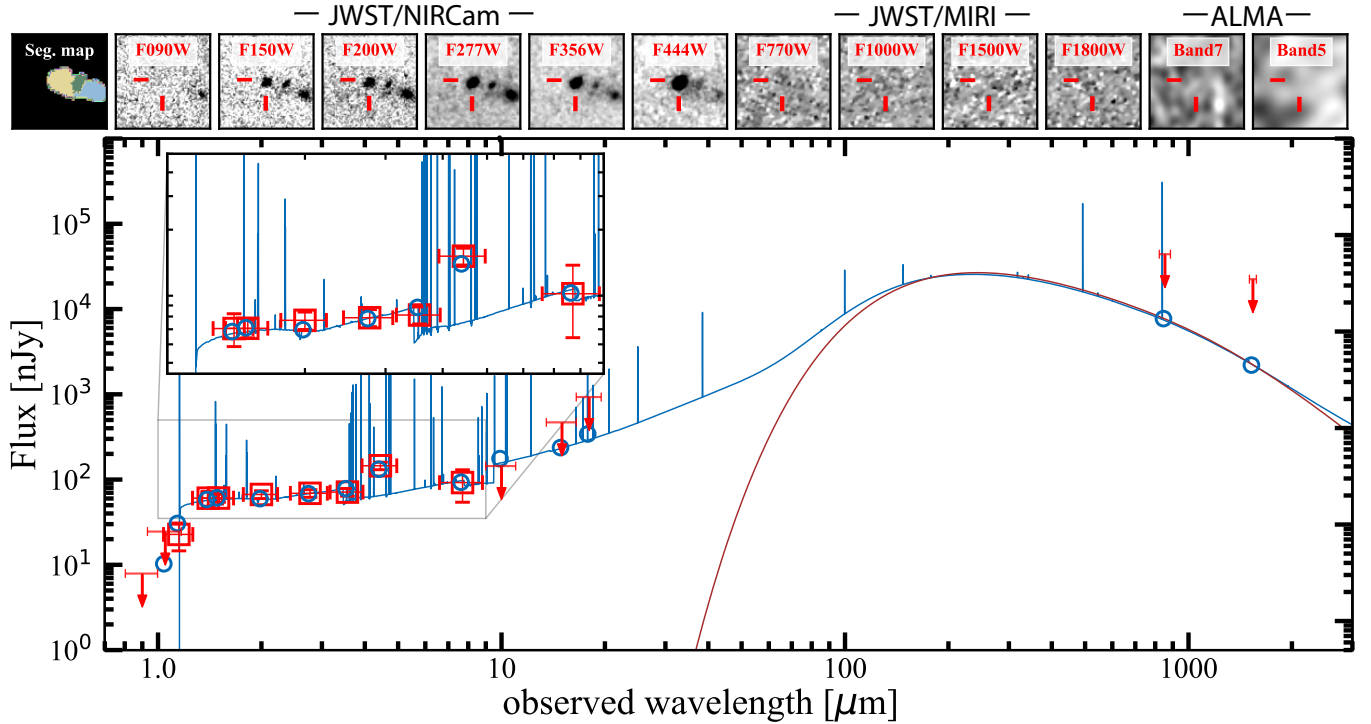


Figure 4. Full SED shape of ID4590 from optical to mm wavelengths in the observed frame. *Top:* $2'' \times 2''$ image cutouts of *JWST/NIRCam*, *JWST/MIRI*, and ALMA from left to right. The red bars indicate the source position of ID4590, and the corresponding filter/Band in each panel is shown in the label. The most-left panel shows the segmentation map from the GRIZLI pipeline. *Bottom:* Blue curve indicates the best-fit SED obtained with CIGALE. The red squares are the observed photometry of ID4590, and the blue circles present the predicted photometry from the best-fit SED. The inset panel zooms in the SED at 1–9 μm , clearly showing the flux boosting in the F444W filter by strong [O III] λ 5007 and H β emission lines, instead of the stellar continuum, where the MIRI photometry helps to disentangle their contributions to the F444W filter. The inset panels also presents the red UV continuum slope ($\beta_{\text{UV}} = -1.7 \pm 0.07$) of ID4590, while the dust continuum is not detected likely because of the high dust temperature (Section 4.3). The brown curve highlights the FIR SED using the Casey (2012) model in CIGALE.

(2023), and we summarize the details of the fitting and parameter ranges used in the fitting in the Appendix.

In the bottom panel of Figure 4, the blue curve shows the best-fit SED, where the brown curve highlights the re-emission of the dust in the rest-frame FIR wavelength based on the Casey (2012) model. The inset panel shows the zoom-in spectrum of the best-fit SED at $\sim 1\text{--}9 \mu\text{m}$. Our best-fit SED reproduces the observed photometry, including the flux enhancement in the F444W filter with the reduced χ^2 value of 0.99. We obtain the best-fit values of $\text{SFR} = 26_{-4}^{+9} M_{\odot} \text{ yr}^{-1}$, $M_{\text{star}} = 5.3_{-2.6}^{+5.6} \times 10^8 M_{\odot}$, UV continuum slope $\beta_{\text{UV}} = -1.70 \pm 0.07$, and $E(B - V) = 0.16 \pm 0.03$ in the observed-frame (i.e. no lens correction), respectively, that are generally consistent with previous NIRcam and/or NIRSpec based measurements (e.g., Carnall et al. 2023; Schaerer et al. 2022; Tacchella et al. 2022), as well as an independent NIRCam and NIRISS based measurements in the separated paper of Heintz et al. (2023). The $\log(L_{\text{IR}}/L_{\odot})$ value is estimated to be 11.2, which is consistent with the upper limit obtained from the independent FIR SED analysis (Section

3.5). This indicates that the current non-detection of the dust continuum with ALMA does not violate the energy balance with the SMC dust attenuation curve, while the β_{UV} and $E(B - V)$ values suggest that ID4590 is a certainly dust-attenuated system, in contrast to very blue galaxies observed in recent *JWST* observations at similar redshifts (e.g., Nanayakkara et al. 2022; Furtak et al. 2022; Cullen et al. 2022; Topping et al. 2022a; Finkelstein et al. 2023; Atek et al. 2022; Fujimoto et al. 2023; Robertson et al. 2022). Note that we confirm that the SED outputs are unchanged beyond 5–10% with and without the ALMA upper limits in the above SED fitting with CIGALE. We further examine the dust and the obscured properties of ID4590 in Section 4.3 and discuss the potential underlying physical mechanisms in Section 4.4.

Because several Balmer emission lines are detected in ID4590 with NIRSpec, we compare our best-fit $E(B - V)$ with the measurement from the Balmer decrement. The line flux measurements from the latest NIRSpec reduction and calibration (Section 2.3) yield $E(B - V) =$

$0.07_{-0.07}^{+0.10}$ and $0.24_{-0.07}^{+0.07}$ from $H\gamma/H\beta$ and $H\delta/H\beta$, respectively, by assuming the SMC dust attenuation law. Our SED-based estimate falls between those estimates from the Balmer decrement approach, suggesting the general consistency between the photometry- and spectroscopic-based approaches. However, caution remains in the different $E(B - V)$ suggested between $H\gamma/H\beta$ and $H\delta/H\beta$, where the difference can change the $H\beta$ -based SFR estimate (e.g., Kennicutt & Evans 2012) by a factor of ~ 3 after the dust correction. We confirm that similarly different $E(B - V)$ values are obtained by assuming other dust attenuation laws (e.g., LMC, Calzetti et al. 2000), and thus the difference is unlikely caused by an improper choice of the dust attenuation law. We speculate that it is caused by the difficulty of the optimal wavelength-dependent slit-loss correction for each emission, taking their potential differential distributions. We thus use the SED-based physical properties in the following analysis.

We note that Giménez-Arteaga et al. (2023) discuss the potential underestimate of M_{star} by ~ 0.5 –1 dex in the spatially-integrated SED analysis, compared to the sum of the spatially-resolved SED analysis, especially in strong optical emission line systems¹³. However, we confirm that our M_{star} estimate is consistent with the results from the spatially-resolved SED analysis in Giménez-Arteaga et al. (2023), owing to the additional constraints from the MIRI bands (Bisigello et al. 2019; Papovich et al. 2023).

4. RESULTS & DISCUSSIONS

4.1. Electron density at $z = 8.5$ via $[O\text{ III}]\lambda 88\mu\text{m}/[O\text{ III}]\lambda 5007$

Owing to the same species and ionized state with different critical densities, the line ratio of $[O\text{ III}]\lambda 88\mu\text{m}/[O\text{ III}]\lambda 5007$ is regulated by the electron density n_e and temperature T_e . In the left panel of Figure 5, we show the line ratio of $[O\text{ III}]\lambda 88\mu\text{m}/[O\text{ III}]\lambda 5007$ as a function of T_e with different assumptions for the electron density n_e , drawn by using the nebular emission code PyNeb¹⁴. The relations show monotonic decreasing functions towards the increase of T_e or n_e . This indicates that we can evaluate n_e with a secure T_e measurement (or vice versa – evaluate T_e with a secure n_e measurement).

¹³ This is because the young bursty stellar populations, causing the strong optical emission lines, dominate the emission in the spatially-integrated photometry, hiding the possible presence of underlying older stellar populations, and yield extremely young ages (< 10 Myr) and therefore lower masses in the SED fit.

¹⁴ <http://research.iac.es/proyecto/PyNeb/>

The NIRSspec observations successfully detect the multiple nebular emission lines from ID4590 in rest-frame UV to optical wavelength, including $[O\text{ III}]\lambda 5007$ and $[O\text{ III}]\lambda 4363$, which provides us with the robust measure of T_e (e.g., Schaerer et al. 2022; Curti et al. 2022; Trump et al. 2022; Heintz et al. 2023; Nakajima et al. 2023). In conjunction with the secure T_e measurement and our ALMA measurements (Section 3.2), we derive the $[O\text{ III}]\lambda 88\mu\text{m}/\lambda 5007$ line ratio for ID4590, and the red circle in the left panel of Figure 5 shows the relation. Based on the 1σ uncertainties, we evaluate $n_e = 220_{-130}^{+230} \text{ cm}^{-3}$.

The n_e value has been typically measured by using density-sensitive line ratios such as $[S\text{ II}]\lambda 6716/6731$, $[O\text{ II}]\lambda 3729/3726$, and $[C\text{ III}]\lambda 1907/1909$ (e.g., Kewley et al. 2019). Previous spectroscopic surveys have found the presence of the redshift evolution of n_e : the typical n_e in local galaxies has increased from $n_e \simeq 30 \text{ cm}^{-3}$ at $z \sim 0$ (e.g., Herrera-Camus et al. 2016) to $n_e \simeq 100$ –200 cm^{-3} at $z \sim 1.5$ (e.g., Kaasinen et al. 2017; Kashino et al. 2017), and to $n_e \simeq 200$ –300 cm^{-3} at $z \sim 2$ –3 (Steidel et al. 2014; Sanders et al. 2016; Davies et al. 2021).

Because of the required high spectral resolution and subsequently high sensitivity to resolve those rest-frame UV and optical doublet lines, the results have been generally limited at $z \lesssim 3$, while recent rest-frame FIR observations have been exploring the n_e measurement even out to the EoR. By using a FIR fine-structure line ratio of $[O\text{ III}]\lambda 52\mu\text{m}$ and $[O\text{ III}]\lambda 88\mu\text{m}$ detected with ALMA, Killi et al. (2022) estimate $n_e < 260 \text{ cm}^{-3}$ in a dusty lensed star-forming galaxy at $z = 7.13$, A1689-zD1 (Watson et al. 2015). Our measurement of a high electron density provides a new determination of n_e at EoR and is consistent with the results in A1689-zD1. For several $z \sim 6$ –9 galaxies with the $[O\text{ III}]\lambda 88\mu\text{m}$ and $[C\text{ II}]\lambda 158\mu\text{m}$ line measurements, Vallini et al. (2021) show that their gas density n_{gas} generally fall within $\simeq 100$ –1000 cm^{-3} by advancing analytical models for these FIR emission lines (Ferrara et al. 2019; Vallini et al. 2020). Although systematic uncertainties remain in this approach due to the C/O abundance and the different emitting regions of the $[O\text{ III}]$ and $[C\text{ II}]$ lines that suggest n_e and n_{gas} are not identical, these n_{gas} measurements at similar redshift also in line with our n_e measurement for ID4590. Our measurement is also broadly consistent with recent NIRSspec measurements for $z \sim 4$ –9 galaxies using the $[O\text{ II}]$ doublet (Isobe et al. 2023a). In contrast, Stark et al. (2017) use the $[C\text{ III}]\lambda 1907/1909$ doublet and estimate $n_e = 9100_{-7800}^{+12200} \text{ cm}^{-3}$ in EGS-zs8-1, a UV-luminous star-forming galaxy at $z = 7.73$, which is much higher than those of our and recent measurements with the $[O\text{ III}]\lambda 88\mu\text{m}$ line.

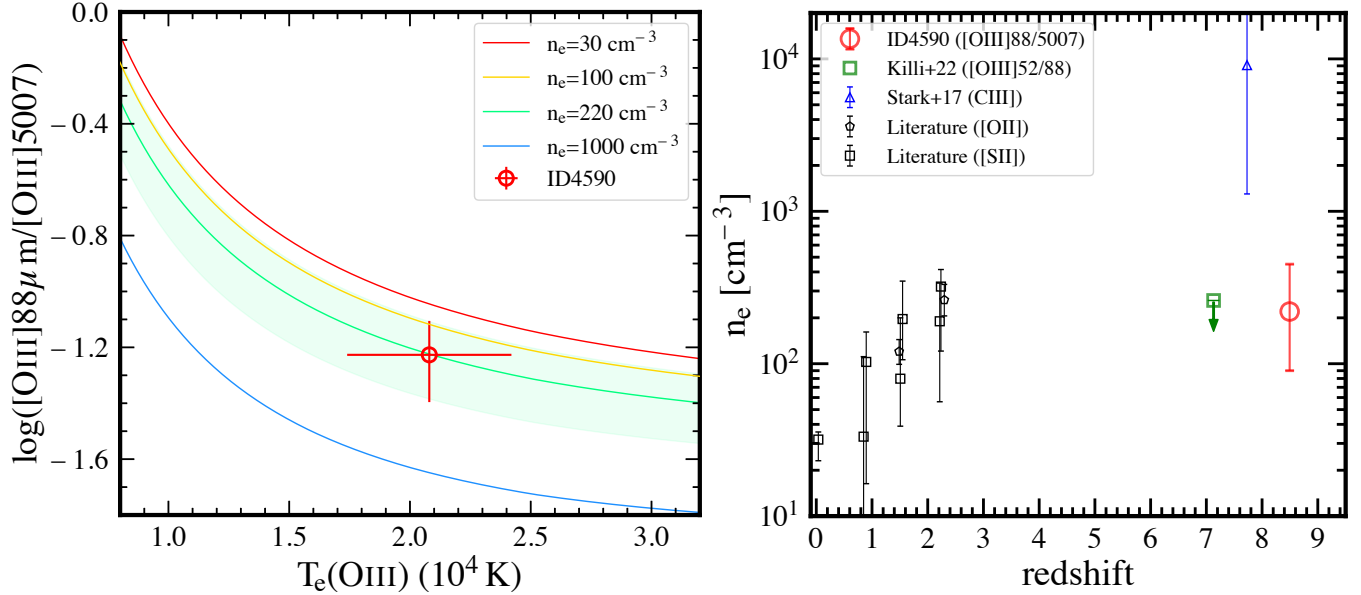


Figure 5. Electron density n_e measurement for ID4590 via the [O III]88 μ m/ λ 5007 line ratio enabled by *JWST* and ALMA. In both panels, the red circles denote ID4590. **Left:** Line ratio as a function of electron temperature T_e with different n_e assumptions, calculated with the nebular emission code *PyNeb*. The green shade presents the 1σ range of the n_e estimate for ID4590. **Right:** Redshift evolution of n_e . The green and blue symbols are the measurements for individual galaxies at the EoR (Killi et al. 2022; Stark et al. 2017), and the black symbols are statistical measurements at $z \sim 0$ –3 taken from literature (Steidel et al. 2014; Sanders et al. 2016; Stott et al. 2016; Kaasinen et al. 2017; Davies et al. 2021).

In the right panel of Figure 5, we summarize the n_e measurement as a function of redshift. The n_e value of ID4590 is similar to $z \sim 2$ –3 star-forming galaxies. This might suggest that the physical mechanisms responsible for driving the high n_e values observed at $z \sim 2$ –3 initially took place in the EoR, and there was a little redshift evolution between $z = 8.5$ and $z \sim 2$ –3, albeit the diversity observed with EGS-zs8-1. However, this redshift trend strongly depends on the galaxy types selected, and similarly high n_e measurements ($\simeq 400 \text{ cm}^{-3}$) are also obtained in compact star-forming galaxies at $z \sim 0.3$ –0.4 (Guseva et al. 2020). Moreover, given the similar high ionization potentials between C III] and [O III]88 μ m emission lines, but much lower critical density of [O III]88 μ m ($\sim 500 \text{ cm}^{-3}$), the different n_e results between the C III] and [O III]88 μ m measurements might indicate these emission lines generally arise from different regions with different n_e values, where we are witnessing the differential n_e distributions inside H II regions. The upcoming *JWST*/NIRSpec observations in the high-resolution spectrograph mode ($R \sim 2700$) will sufficiently resolve the rest-frame UV and optical doublet lines, statistically evaluate n_e based on a mass-complete sample, verify the presence of its redshift evolution and/or differential n_e distributions traced by different emission lines, and determine what key mechanisms regulate n_e out to the EoR.

4.2. SFR– $L_{\text{[CII]}}$, $L_{\text{[OIII]}}$, and $L_{\text{[OIII]}}/L_{\text{[CII]}}$ Relations

In Figure 6 and 7, we present $L_{\text{[CII]}}$, $L_{\text{[OIII]}}$, and $L_{\text{[OIII]}}/L_{\text{[CII]}}$ as a function of SFR for ID4590. We show the results after the lens correction, where the systematic uncertainty of 30% for the magnification factor (Section 3.1) is propagated in the error bars. In SFR– $L_{\text{[CII]}}$ (SFR– $L_{\text{[OIII]}}/L_{\text{[CII]}}$) relation, we also show the 3σ upper limit (lower limit) for $L_{\text{[CII]}}$ ($L_{\text{[OIII]}}/L_{\text{[CII]}}$) at the *JWST* source position, given its spatial offset (Section 3.4), and separate the results inside and outside the galaxy with filled and open circles, respectively. For comparison, we also present compilations of recent ALMA results for $z \sim 6$ –9 galaxies in literature (e.g., Harikane et al. 2020; Fujimoto et al. 2021) with black squares, and local dwarf galaxy results with the gas-phase metallicity (Z_{gas}) measurements (De Looze et al. 2014; Cormier et al. 2015) with color circles. The color scale is equal to $12 + \log(\text{O}/\text{H})$ denoted in the color bar, except for the $z \sim 6$ –9 galaxy results whose Z_{gas} values have not been constrained. The average relation for the local dwarf galaxies is shown in the dashed black line with the 1σ range in the grey shade. In all relations, ID4590 are generally consistent with the results estimated in other $z \sim 6$ –9 galaxies. In addition, ID4590 explores the faint-end of the $z \sim 6$ –9 galaxy results, owing to the aid of the gravitational lensing effect. Therefore, ID4590 is a faint, thus abundant, and representative early galaxy

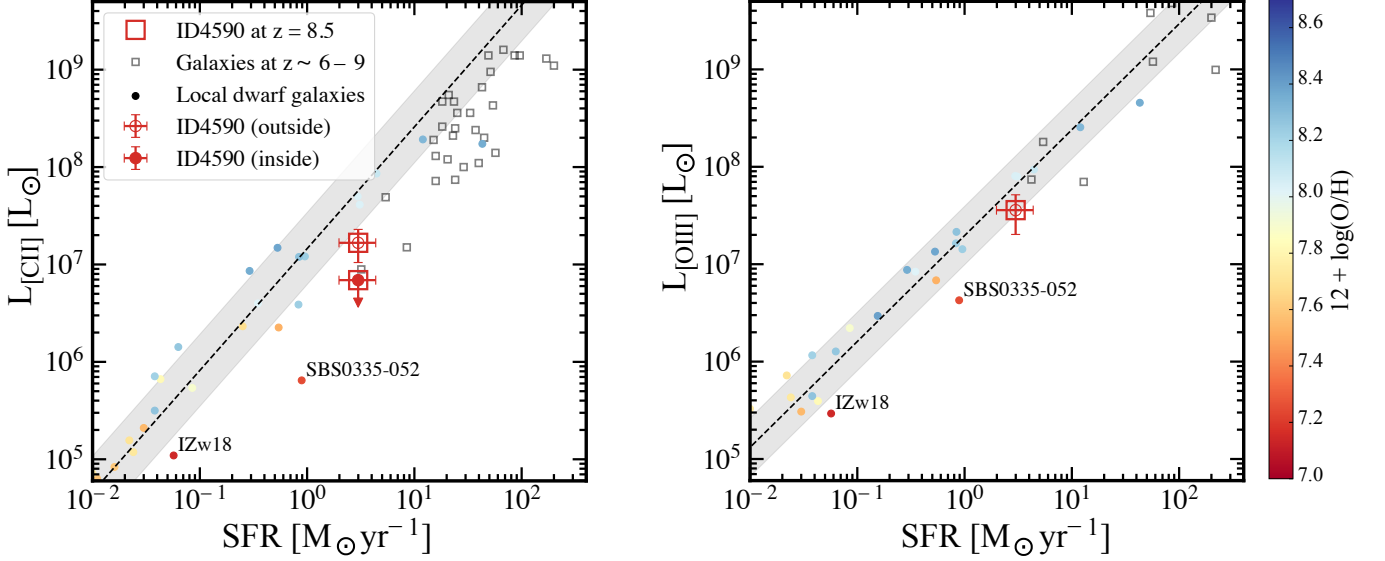


Figure 6. Relations between SFR and $L_{[\text{CII}]}$ (left) and $L_{[\text{OIII}]}$ (right). In both panels, the color of the circles corresponds to the gas-phase metallicity Z_{gas} denoted in the color bar. The open red squares remark the measurements of ID4590, where the filled and open circles indicate the measurements inside and outside the galaxy. The red arrows present the 3σ upper limit of $[\text{CII}]$ at the *JWST* source position given its spatial and velocity offsets (Section 3.2). We assume that the $[\text{CII}]$ -detected gas outside the galaxy is illuminated by ionizing photons escaping from the galaxy and thus use the same SFR value for both results of inside and outside the galaxy. Other color circles represent the local dwarf galaxies with the Z_{gas} measurements (De Looze et al. 2014; Cormier et al. 2015), where the best-fit relation and its 1σ dispersion is shown with the dashed line and the grey-shaded area, respectively. The open black squares show the results for $z \sim 6-9$ galaxies compiled in Harikane et al. (2020).

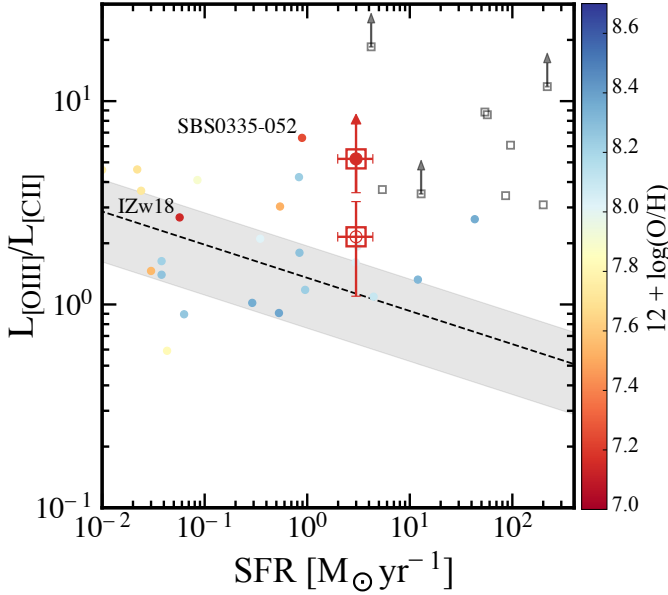


Figure 7. Same as Figure 6, but for $L_{[\text{OIII}]} / L_{[\text{CII}]}$. ID4590 shows a high $L_{[\text{OIII}]} / L_{[\text{CII}]}$ ratio of > 4 at the galaxy position similar to those of known $z \sim 6-9$ galaxies.

with physical properties similar to other galaxies so far observed with ALMA at similar redshifts. This indicates that ID4590 is a unique laboratory to study what

regulates the FIR major coolant lines of $[\text{CII}]158\mu\text{m}$ and $[\text{OIII}]88\mu\text{m}$ in EoR galaxies.

In the SFR– $L_{[\text{CII}]}$ relation, we find that ID4590 falls below the typical relation of the local dwarf galaxies in both results obtained inside and outside the galaxy. Among the local dwarf galaxies, there are two galaxies of IZw18 and SBS0335-052 whose Z_{gas} measurements are similarly low as ID4590 ($12 + \log(\text{O}/\text{H}) \simeq 7.1-7.3$). We confirm that the $\log(L_{[\text{CII}]} / \text{SFR})$ ratio inside the galaxy shows < 6.3 , which is consistent with these two very metal-poor local galaxies (~ 5.7). This might indicate that the low $[\text{CII}]$ line emissivity of ID4590 is explained by the low Z_{gas} ISM condition (e.g., Vallini et al. 2015), while there are also other key factors which reduce the $[\text{CII}]$ emissivity such as high ionization parameter or low gas density (see Section 1). In fact, ID4590 shows strong $[\text{OIII}]\lambda 5007 + \text{H}\beta$ emission (Section 3.6), which generally represents recent young bursty stellar populations (e.g., Topping et al. 2022b; Witstok et al. 2022), where the high ionization parameter, as a result, might be a more critical driver. The $[\text{CII}]$ emission outside the galaxy shows $\log(L_{[\text{CII}]} / \text{SFR}) \sim 6.7$, being higher than these very metal-poor local galaxies but still lower than the typical relation. This might be explained by a huge amount of gas around ID4590 which efficiently uses all the photons to boost the $[\text{CII}]$

emission eventually. With an analytical model, Ferrara et al. (2019) predict that the surface density of [C II] luminosity becomes almost constant around $\Sigma_{[\text{C II}]} \approx 10^6 - 10^7 L_{\odot} \text{ yr}^{-1} \text{ kpc}^{-1}$ at a high SFR surface density regime of $\Sigma_{\text{SFR}} \gtrsim 10 M_{\odot} \text{ yr}^{-1} \text{ kpc}^{-2}$ with a linear scale dependence on the gas density, regardless of Z_{gas} in 0.1–1.0 Z_{\odot} (see eq. 42 in Ferrara et al. 2019). Based on our size and full SED analyses in Section 3, ID4590 indeed shows $\Sigma_{[\text{C II}]} \simeq 2 \times 10^6 L_{\odot} \text{ yr}^{-1} \text{ kpc}^{-2}$ with $\Sigma_{\text{SFR}} \simeq 100 M_{\odot} \text{ yr}^{-1} \text{ kpc}^{-2}$, which agrees with the prediction from the analytical model. For more discussions related to the rich gas aspect around ID4590, we refer the reader to a separate paper by Heintz et al. (2023).

In the SFR– $L_{[\text{O III}]}$ relation, we find that ID4590 is consistent with the local relation within the errors but likely falls slightly below it. This would also be explained by the low [O III] line emissivity with low Z_{gas} values (e.g., Popping 2022), which is also shown in the monotonic decreasing function in the [O III]88/[O III] $\lambda 5007$ – T_e relation, regardless of n_e (Figure 5). In fact, the slightly low $\log(L_{[\text{O III}]}/\text{SFR})$ ratio of ID4590 is consistent with those of the two very metal-poor local galaxies of IZw18 and SBS0335-052 (~ 6.5) within the errors. We also confirm that the SFR– $L_{[\text{O III}]}$ relation of ID4590 is consistent with the SERRA zoom-in simulation results (e.g., Pallottini et al. 2022; Kohandel et al. 2022) for galaxies whose $\log(U)$ values are similar to that of ID4590 ($\log(U) > -2.27$; Section 2.3).

In the SFR– $L_{[\text{O III}]} / L_{[\text{C II}]}$ relation, we find that ID4590 shows higher $L_{[\text{O III}]} / L_{[\text{C II}]}$ ratios both inside and outside the galaxies than the local relation. In particular, the lower limit of > 4 obtained inside the galaxy is similarly high to other $z \sim 6$ –9 galaxies so far observed (e.g., Harikane et al. 2020; Witstok et al. 2022). We discuss the physical origins of the high [O III]/[C II] line ratio in Section 4.5.

4.3. IRX– β relation

Figure 8 presents the infrared excess ($L_{\text{IR}}/L_{\text{UV}} \equiv \text{IRX}$) and the UV continuum slope β_{UV} relation of ID4590. Although we adopt the fiducial value of $T_{\text{d}} = 60 \text{ K}$ in Section 3.5, here we show two extreme cases for ID4590, with $T_{\text{d}} = 30 \text{ K}$ and 90 K , by assuming the potential uncertainty of $\Delta T_{\text{d}} = \pm 30 \text{ K}$. For comparison, we also show the relations based on several dust attenuation laws (Reddy et al. 2018; Calzetti et al. 2000), a

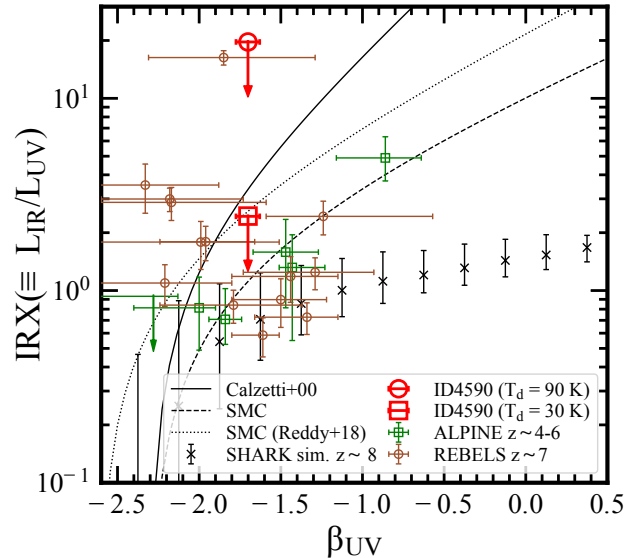


Figure 8. IRX– β_{UV} relation. The red symbols represent ID4590, where the square and the circle show the upper limits with the T_{d} assumptions of 30 K and 90 K, respectively. The solid and dashed curves indicate the relations derived with the dust attenuation of SMC and Calzetti et al. (2000), respectively. The dotted curve shows the relation derived from SMC dust attenuation and bluer intrinsic β_{UV} (Reddy et al. 2018). For comparison, we also show other star-forming galaxy results at $z \sim 4$ –7 taken from ALPINE (green squares; Le Fèvre et al. 2020; Fudamoto et al. 2020) and REBELS (brown circles; Bouwens et al. 2021; Inami et al. 2022). The black crosses indicate semi-analytical simulation results of SHARK (Lagos et al. 2020), for galaxies at $z \sim 8$ with $\log(M_{\text{star}}/M_{\text{star}}) = 7.5$ –8.5, where the error bars are the 16–84th percentile.

semi-analytical model of SHARK¹⁵ for galaxies at $z \sim 8$ (Lagos et al. 2020), and the recent measurements for $z \sim 4$ –7 star-forming galaxies observed in the ALPINE (Le Fèvre et al. 2020) and REBELS surveys (Bouwens et al. 2021) taken from Fudamoto et al. (2021) and Inami et al. (2022), respectively. While several Balmer emission lines are detected in ID4590, we note that concluding which dust attenuation law fits the best with ID4590 is still challenging with their current S/N and the potential difficulty of the proper aperture correction for each Balmer emission (Section 3.6).

In Figure 8, ID4590 falls in a moderately red UV color regime, where the dust continuum is detected from the previous ALMA observations for the $z \sim 4$ –7 galaxies. If ID4590 has a relatively low T_{d} (~ 30 –40 K) and follows

¹⁵ The dust extinction and re-emission are modeled with Charlot & Fall (2000) and the templates of Dale et al. (2014), respectively, while the final IRX– β_{UV} relation is also regulated by dust surface density, Z_{gas} , M_{gas} , and galaxy structure.

a dust attenuation law similar to Calzetti et al. (2000) or SMC in Reddy et al. (2018), the upper limit suggests that the dust continuum should be detected from ID4590 with the current ALMA depth¹⁶. This indicates that ID4590 has a T_d value higher than ~ 30 – 40 K or an SMC-like steep dust attenuation law with the intrinsic UV continuum slope of $\beta_{UV,0} \simeq -2.3$ (e.g., Meurer et al. 1999; McLure et al. 2018). Given the low dust content implied from the low metallicity of ID4590 from the NIRSpec results (Section 2.3) and the high Σ_{SFR} from the compact rest-frame UV size (Section 3.3), the dust is efficiently heated at a given UV field (e.g., Behrens et al. 2018; Sommovigo et al. 2022b,a), and the former high T_d scenario might be plausible. We also find that the semi-analytical model of SHARK predicts the IRX– β_{UV} relation even lower than the SMC relation for the simulated galaxies with similar redshift and M_{star} as ID4590, the non-detection of the dust could be simply because of the difference of the dust attenuation law between local and high- z galaxies.

Future ALMA high-frequency follow-up observations (e.g., Band 8, 9, and 10) will confirm or rule out the high T_d scenario in ID4590. Furthermore, the detection of the rest-frame UV–optical continuum and/or multiple high-significance detection of Balmer and Paschen emission lines in upcoming JWST/NIRSpec and MIRI observations will help us to directly constrain the dust attenuation curve in high-redshift galaxies, including ID4590.

4.4. Onset of outflow at $z > 8.5$, facilitating reionization

In Figure 2, we find the spatial offset of [C II] from the JWST source position (Section 3.4). The spatial offset suggests the presence of the accreting/satellite gas clump(s) (e.g., Maiolino et al. 2015) or the extended [C II] gas beyond the stellar distribution (e.g., Fujimoto et al. 2019, 2020; Ginolfi et al. 2020; Carniani et al. 2020; Herrera-Camus et al. 2021; Akins et al. 2022; Lambert et al. 2022), tracing the diffuse neutral hydrogen (Heintz et al. 2021, 2022). The [C II] size measurement result, almost ~ 10 times larger than the stellar distribution of ID4590 (Section 3.3), supports the latter scenario of the presence of the extended [C II] gas. Although we cannot rule out the possibility that the noise fluctuation makes the [C II] morphology look extended with the current S/N, it is worth mentioning that similarly extended [C II] morphology with spatial offsets have also been observed

in other galaxies at $z \sim 7$ – 9 (Carniani et al. 2020). The other possibility could be nearby faint, dusty objects (e.g., Fujimoto et al. 2016, 2022) emitting [C II] (e.g., Romano et al. 2020; Fudamoto et al. 2022b). However, no counterparts are identified down to a 3σ upper limit in F150W of ~ 32.5 mag (with $0''.2$ -diameter; Harikane et al. 2022) after the lens correction, which corresponds to $SFR \approx 0.05 M_\odot \text{ yr}^{-1}$ at $z = 8.5$ (e.g., Kennicutt & Evans 2012). Similarly, no counterparts in F444W place a 3σ upper limit of $M_{star} \lesssim 1 \times 10^6 M_\odot$ by scaling the best-fit SED of ID4590. A pixel-based SED analysis in Giménez-Arteaga et al. (2023) shows the gradient of the dust obscuration decreasing towards the [C II]-emitting region, which also supports the absence of the counterparts at the [C II] peak position.

Whichever the [C II]-emitting gas is compact clump(s) diffuse & extended, these results suggest that the carbon in the gas is illuminated not by local star-forming activities, but by i) the ionizing photon escaped from inside the galaxy, ii) shock heating of the outflowing gas, or iii) a cooling process of the hot outflowing gas (see also discussions in e.g., Fujimoto et al. 2019, 2020; Pizhati et al. 2020; Akins et al. 2022). In Figure 6, we find that the $L_{[CII]}/SFR$ ratio of this [C II] emission outside of galaxy is consistent with other local dwarf galaxies whose Z_{gas} values are similarly low as ID4590 (IZw18 and SBS0335-052). This suggests that the input energy from i) is enough to explain the observed $L_{[CII]}$. In fact, the high ionization parameter of $\log(U) \gtrsim -2$ observed in ID4590 is in line with the scenario of i).

In Figure 2, we also find the extended ionized gas ([O III] $\lambda 5007$, H β) structure in the deep NIRCam/F444W filter (Section 3.4). Similar to the [C II] emission, no NIRCam counterparts are identified in the extended ionized gas regions. In addition, the extended ionized gas regions are also not matched with the direction of the high dust obscuration gradient, which denies the possibility that the obscured star-forming regions cause the extended ionized emission. Based on the size measurement results in the image plane (Section 3.3) and the different radial and tangential magnifications (see middle panel of Figure 2), the ionized [O III] $\lambda 5007$ +H β structure extends out to > 8 times more than the effective radius of the stellar distribution of ID4590 (Section 3.4). Same as [C II], i)–iii) are the possible physical origins of the extended ionized gas emission. Interestingly, from the center of ID4590, the regions of the extended ionized gas distribution (\sim Southeastern) and the peak position of the [C II] emission (\sim Northern) are in different directions. This might indicate that the differential distributions of the nebular parameters, such as n_e , Z_{gas} , $\log(U)$, and C/O

¹⁶ In the energy balance between the dust attenuation and re-emission, a lower T_d makes the FIR SED peak wavelength longer at a given L_{IR} , where the ALMA sensitivity limit may reach the FIR SED peak at some point.

abundance cause these differential distributions, even if the same physical process is taking place, either of i)–iii). The different morphology between [O III]88 μ m and [O III]5007+H β might also be attributed to the differential distributions of the nebular parameters, although the insufficient depth in the ALMA 88 μ m map could be another plausible cause.

Importantly, regardless of the true physical processes to give rise to an offset-[C II] and extended [O III]5007+H β gas emission, the presence of the metal-enriched gas away from the galaxy is strong evidence of past and/or ongoing outflow activities already taking place in a low-mass ($M_{\text{star}} = 6 \times 10^7 M_{\odot}$), metal-poor ($Z = 0.04Z_{\odot}$) nascent galaxy at $z = 8.496$. The presence of the extended carbon gas structure, so-called [C II] Halo, has been reported around more massive ($M_{\text{star}} > 10^9\text{--}10^{10} M_{\odot}$) star-forming galaxies at $z = 4 - 7$ (e.g., Fujimoto et al. 2019, 2020; Ginolfi et al. 2020; Herrera-Camus et al. 2021; Akins et al. 2022; Lambert et al. 2022), which is challenging to the current cosmological galaxy formation models (Fujimoto et al. 2019; see also e.g., Pizzati et al. 2020; Arata et al. 2020; Katz et al. 2022). Our results in ID4590 provide new insight that such metal enrichment beyond the galaxy ISM scale starts to occur even in the very early phase of the galaxy assembly just ~ 580 Myr after the Big Bang, which is likely linked to the origin of the [C II] halo at a later epoch of the Universe.

Another important fact is that the presence of diffuse extended ionized gas around ID4590 directly indicates the high filling factor of the ionized gas, where the ionizing photons escaping from the galaxy may contribute to the Reionization. After the lens correction, ID4590 is $\sim 5\times$ fainter than the characteristic UV luminosity of the UV luminosity function (UVLF) at $z \sim 9$ ($M_{\text{UV}}^* = -19.6$ mag; e.g., Harikane et al. 2022). Once we confirm the high escape fraction of the ionizing photons from faint, low-mass galaxies, probably related to the onset of the outflow from the early stage of the galaxy assembly, it also provides us with a new insight into the process of the Reionization, in contrast to the scenario that huge ionized bubbles are formed around UV-bright galaxies ($M_{\text{UV}} \lesssim -22$) at similar redshifts (e.g., Mason et al. 2018). The significantly low metallicity of ID4590, falling below the $z \sim 8$ mass–metallicity relations predicted from current galaxy formation models (e.g., Curti et al. 2022), despite the dust obscuration in ID4590 ($\beta = -1.7 \pm 0.07$), may suggest that dust obscuration occurs in a part of the galaxy with a very low dust content. This may also be caused by the past or ongoing outflow activities (Ferrara et al. 2022; Ziparo et al. 2022) that carry the dust away from the galaxy

and make it diffuse, cold, and undetectable in the observations (e.g., Akins et al. 2022), while the dust in regions that are not invested by the outflow, or that are shielded by Giant Molecular Clouds, could survive (see also Martínez-González et al. 2019; Nath et al. 2022). This small amount of surviving dust may be responsible for a certain amount of dust obscuration. In any case, the low dust content in the galaxy is also helpful for ionizing photons to escape from the system.

Note that diffuse ionized gases (DIGs) have been observed in local galaxies, from inter-arm regions (e.g., Zurita et al. 2000) to areas above the galactic mid-plane out to 1–2 kpc scales (e.g., Rossa & Dettmar 2000). However, even in the latter case, the sizes of these DIGs are only about $\sim 10\%$ relative to the size of the host galaxy (e.g., Rossa & Dettmar 2003). In contrast, the extended ionized gas structure around ID4590 is well beyond the central galaxy size (Section 3.4). Therefore, the physical origins of the extended ionized gas structure around ID4590 are likely different from those of the DIGs in the local Universe.

Another note is that we do not find evidence of the ongoing outflow via the broad-wing feature in the NIRSpec spectrum. However, the slit of the NIRSpec MSA is aligned perpendicular to the extended ionized gas structure (See the white rectangle in Figure 2), which might be the reason for the absence of the broad-wing feature in the current NIRSpec spectrum.

4.5. Physical origins of the high [O III]88 μ m/[C II]158 μ m ratio

Previous ALMA observations reported the detections of the luminous [O III]88 μ m line from star-forming galaxies at $z \sim 6\text{--}9$, showing their [O III]88 μ m/[C II]158 μ m line ratio of $\gtrsim 3\text{--}10$ that are higher than local dwarf galaxies and/or local Luminous Infrared Galaxies (LIRGs) with similar SFRs (Inoue et al. 2016; Harikane et al. 2020; Witstok et al. 2022). The origin of such high ratios is still unclear. Major solutions that have been argued include a) observational bias (e.g., Carniani et al. 2020), b) low C/O abundance ratio (Katz et al. 2022), c) low covering fraction of PDRs¹⁷ C_{PDR} (Cormier et al. 2015; Harikane et al. 2020), and d) the characteristic ISM parameters in early galaxies such as the high ionization parameter (Katz et al. 2017; Harikane et al. 2020) probably caused by recent strong bursts of star-formation (Ferrara et al. 2019; Arata et al. 2020; Vallini et al. 2021; Witstok et al. 2022; Sugahara et al. 2022)

¹⁷ This is equal to the high filling factor of the ionized gas relative to dense PDRs.

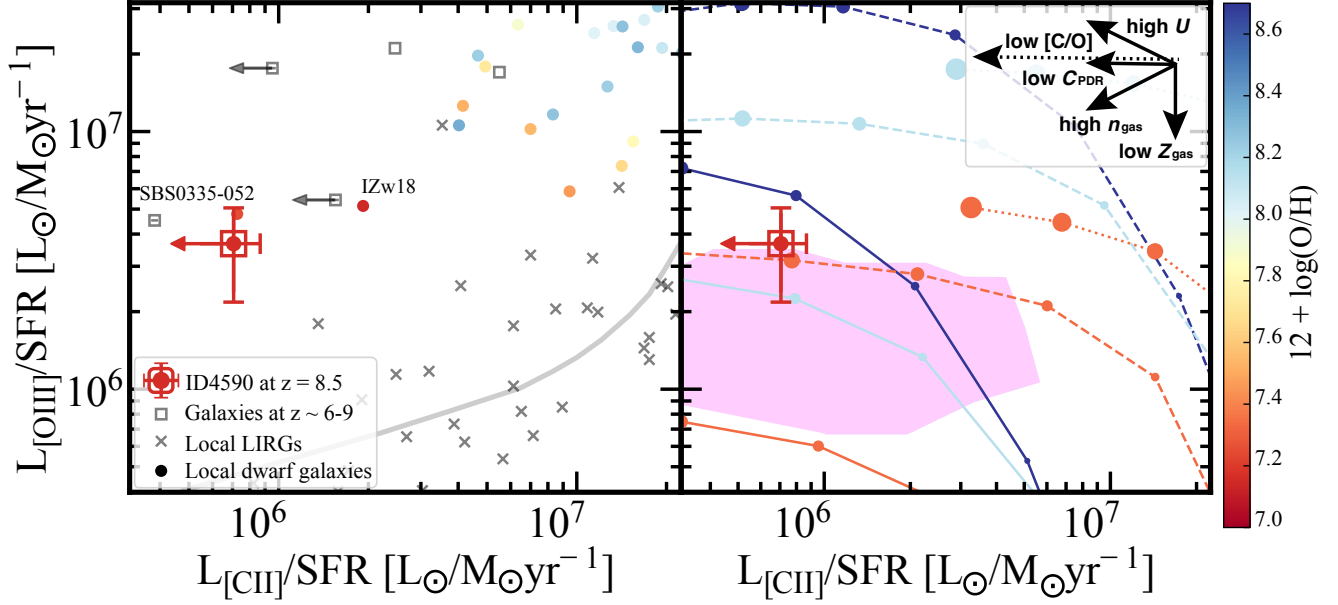


Figure 9. FIR line diagnostic of $L_{[\text{OIII}]}/\text{SFR}$ and $L_{[\text{CII}]}/\text{SFR}$, produced in the same manner as Figure 12 in Harikane et al. (2020). **Left:** The relation from the observations. The color and symbols represent the same as Figure 6. The grey crosses are newly added in this panel, showing the local LIRGs (Howell et al. 2010; Díaz-Santos et al. 2017) whose SFR values are comparable to $z \sim 6-9$ galaxies in the panel. The grey curve is the typical relation for the local LIRGs. **Right:** Same as the left panel, but comparing with CLOUDY calculations. The magenta-shaded region represents the possible parameter space for ID4590 calculated with CLOUDY based on its best-fit nebular parameters of $Z_{\text{gas}} = 0.04 \pm 0.02$, $n_e = 220_{-130}^{+230} \text{ cm}^{-3}$, $\log(U) > -2.27$, and $\log(\text{C}/\text{O}) = [-0.52 : -0.26]$ constrained by our joint *JWST* and ALMA analysis. For comparison, we also show the relations with different parameter sets; the orange, dark light blue, and dark blue lines are the results with $Z_{\text{gas}} = 0.05, 0.1$, and $1.0 Z_{\odot}$; the dotted, dashed, and solid lines correspond to densities of $\log(n_{\text{gas}}/[\text{cm}^{-3}]) = 0.5, 2.0$, and 3.0 ; and the larger circles indicate higher ionization parameters, from $\log U = -4.0$ ion to -0.5 with a step size of 0.5 . The black arrows in the inset panel show directions and possible shifts in the $L_{[\text{OIII}]}/\text{SFR} - L_{[\text{CII}]}/\text{SFR}$ plane due to the physical mechanisms of b), c), and d). To perform a fair comparison, we use the SFR value based on the dust-corrected $\text{H}\alpha$ luminosity in the same manner as Harikane et al. (2020), instead of the SED based estimate. Using $\text{H}\alpha$ luminosity is also beneficial to count the ionizing photons contributing to the line emissivities more directly.

and/or low stellar-to-gaseous metallicity ratio (Sugahara et al. 2022).

In Section 6, we find that ID4590 also shows a similarly high $[\text{O III}]88\mu\text{m}/[\text{C II}]158\mu\text{m}$ line ratio of > 4 at the galaxy position. In addition to the accurate measures of Z_{gas} and n_e (Section 4.1), the deep NIRSspec observations also cover the $[\text{O II}]3729$ and $[\text{C III}]1909$ emission lines from ID4590, which allow us to constrain the ionization parameter $\log(U)$ (e.g., Schaerer et al. 2022; Curti et al. 2022; Brinchmann 2022; Trump et al. 2022; Heintz et al. 2023; Nakajima et al. 2023) and the C/O abundance in ID4590 (e.g., Arellano-Córdova et al. 2022; Isobe et al. 2023b). This indicates that we can investigate the physical origins of the high $[\text{O III}]88\mu\text{m}/[\text{C II}]158\mu\text{m}$ line ratio, taking the possible solutions of b) and d) into account via the actual observed measurements for ID4590. Besides, the spatial offset of the $[\text{C II}]$ line (Section 3.4) allows us to separate the emission arising inside and outside the galaxy and fairly compare the line ratio, also managing the ob-

servational bias of point a). Therefore, with this best optical-mm characterization of an early galaxy owing to the joint *JWST* and ALMA analysis, we are ready to address the physical origins of the high $[\text{C II}]/[\text{O III}]$ and verify whether the remaining possible solution of c) is critical or other solutions can answer already.

In Figure 9, we show the $L_{[\text{OIII}]}/\text{SFR}$ and $L_{[\text{CII}]}/\text{SFR}$ relation of ID4590. Given the purpose of the analysis, we use the $[\text{C II}]$ results at the galaxy position. For comparison, we also present the relations from observations (left panel) and the predictions from the photoionization model with CLOUDY (right panel) drawn in the same manner as Harikane et al. (2020) (see also Sugahara et al. 2022), where the possible shifts on the plane by b), c), and d) are presented with black arrows (Harikane et al. 2020). We also show the magenta-shaded region that corresponds to the possible space for ID4590 calculated by CLOUDY with our fiducial estimates of $Z_{\text{gas}}/Z_{\odot} = 0.04 \pm 0.02$, $n_e = 220_{-130}^{+230} \text{ cm}^{-3}$, $\log(U) > -2.27$, and $\log(\text{C}/\text{O}) = [-0.52 : -0.26]$. Fol-

lowing Harikane et al. (2020), we use the SFR value based on the dust-corrected $H\alpha$ luminosity estimated from NIRSspec (Section 2.3), instead of the SED-based value, for this analysis.

In the left panel, we find that ID4590 shows the $L_{[\text{O III}]}/\text{SFR}$ ratio much higher than local LIRGs, falling on the high $[\text{O III}]/[\text{C II}]$ line ratio regime similar to other $z \sim 6-9$ galaxies. We also find that several metal-poor galaxies ($12+\log(O/H) \lesssim 8.0$) among the local dwarf galaxies are located in the similarly high $[\text{O III}]/[\text{C II}]$ line ratio regime to these $z \sim 6-9$ galaxies. This may suggest that the ISM conditions of these $z \sim 6-9$ galaxies are similar to those of the local metal-poor galaxies, while an important note is that these local metal-poor galaxies have much lower SFRs than these $z \sim 6-9$ galaxies by $\sim 1-2$ orders of magnitudes.

In the right panel, we find that the observed $L_{[\text{O III}]}/\text{SFR}$ and $L_{[\text{C II}]}/\text{SFR}$ relation of ID4590 is consistent with the magenta-shaded region within the errors. This indicates that the $[\text{C II}]$ and $[\text{O III}]$ emissivities at a given input energy in ID4590 are generally explained by the combination of high $\log(U)$, high n_e , low Z_{gas} , and low $\log(C/O)$. Therefore, the physical origin of the high $[\text{O III}]/[\text{C II}]$ ratio observed among $z \sim 6-9$ galaxies may be sufficiently explained by b) and d).

As discussed in Harikane et al. (2020), another possible origin of c) – the low C_{PDR} – could also be the additional reason to boost the $[\text{O III}]/[\text{C II}]$ ratio. As indicated in the black arrow, this effect makes the data points horizontally to move to the left in Figure 9 (i.e., towards low $[\text{C II}]/\text{SFR}$). Because the current $\log(U)$ estimate provides the upper limit alone, the possible parameter space of ID4590 extends to the low $L_{[\text{C II}]}/\text{SFR}$ regime, where we cannot disentangle the contributions from $\log(U)$ and C_{PDR} . Once the upper boundary of $\log(U)$ is constrained, the lower limit of the $L_{[\text{C II}]}/\text{SFR}$ ratio in the possible parameter space will be determined, where the additional C_{PDR} contribution will be evaluated if the observed $L_{[\text{C II}]}/\text{SFR}$ upper limit is lower than the possible parameter space. With future deep $[\text{C II}]$ follow providing a much more stringent upper limit or the faint detection of $[\text{C II}]$, we may be able to investigate further the additional contribution from C_{PDR} .

5. SUMMARY

In this paper, we present the ALMA Band 7 and Band 5 deep spectroscopy for the two major coolant FIR lines of $[\text{O III}]88 \mu\text{m}$ and $[\text{C II}]158 \mu\text{m}$ from ID4590, a metal-poor, low-mass, strongly lensed sub- L^* galaxy at $z = 8.496$, whose warm interstellar medium and stellar properties have been the best characterized with the *JWST* Early Release Observations (ERO) for the

SMACS0723 field. The *JWST* ERO observations include the deep imaging with NIRCcam and MIRI at $\sim 1-20 \mu\text{m}$ as well as deep spectroscopy with NIRSspec at $\sim 2-5 \mu\text{m}$ which detects multiple rest-frame optical emission lines, including $[\text{O III}]\lambda 4363$ line, and provides us with the robust measure of the gas-phase metallicity via the *direct* temperature method for the first time at $z \gtrsim 3$. Combining these rich *JWST* data with *HST* and ALMA, the high-spatial-resolution, homogeneous data set from optical to mm wavelengths enables us to perform a panchromatic characterization of an early galaxy in and out, which sets the benchmark for synergetic studies of ALMA and *JWST* in the coming decades. The main findings of this paper are summarized as follows:

1. We detect both $[\text{C II}]158\mu\text{m}$ and $[\text{O III}]88\mu\text{m}$ lines at 4.0σ and 4.5σ levels, respectively. The redshift and the spatial position of the $[\text{O III}]$ line exactly coincide with those of the *JWST* source. On the other hand, the $[\text{C II}]$ line is blue-shifted by 90 km s^{-1} and has a spatial offset by $\sim 0''.5$ ($\approx 0.5 \text{ kpc}$ in source plane) beyond the errors, where the chance projection of the noise fluctuation is very unlikely ($\sim 0.07\%$) from a blind line search analysis in the same data cube. This indicates that $[\text{C II}]$ velocity and spatial offsets are real and associated with some physical mechanisms of ID4590.
2. We evaluate the sizes of $[\text{C II}]$, $[\text{O III}]$, rest-frame UV, and rest-frame optical continuum by using ALMA and *JWST*/NIRCcam images. With the 2D profile fitting in the image plane, we obtain the best-fit circularized effective radii of $0''.69 \pm 0''.42$, $0''.056 \pm 0''.012$, and $0''.059 \pm 0''.010$ for $[\text{C II}]$, rest-frame UV, and rest-frame optical continuum, respectively. The $[\text{O III}]$ line is not spatially resolved with the current resolution and sensitivity, and we place its upper limit of $0''.16$. We find that the position angle estimated in the F150W filter shows an excellent agreement with the lensing distortion predicted from the mass model, validating the high magnification of $\mu = 8.69$ in ID4590. The extended $[\text{C II}]$ distribution relative to the stellar continuum is reminiscent of the $[\text{C II}]$ Halo reported in recent ALMA studies, while we cannot exclude the possibility that the $[\text{C II}]$ size estimate is affected by the noise fluctuation with the current S/N.
3. The dust continuum is not detected in neither Band 7 or Band 5, and we place 2σ upper limits of $41.8 \mu\text{Jy}$ and $23.2 \mu\text{Jy}$ at 0.85 mm and 1.54 mm , respectively. By assuming a single modified black body with the dust temperature $T_d = 60 \text{ K}$ and

the dust spectral index of $\beta_d = 1.8$, we estimate the upper limits of infrared luminosity over 8–1000 μm of $L_{\text{IR}} < 1.8 \times 10^{10} L_{\odot}$ and the dust mass of $M_{\text{dust}} < 1.2 \times 10^5 M_{\odot}$ after the lens correction, while a different T_d assumption by ± 30 K changes these constraints by $\sim \pm 0.5$ –1.0 dex. The upper limit of infrared excess ($\text{IRX} \equiv L_{\text{IR}}/L_{\text{UV}}$) in ID4590 suggests that T_d is higher than 30–40 K or that steep dust attenuation laws similar to SMC are favored.

4. The NIRCcam/F444W filter, including the contributions from [O III] $\lambda 5007$ and H β emission lines, shows an extended structure where the rest-frame UV and optical continuum are invisible and the 3σ upper limit in the rest-frame UV continuum after the lens correction are placed at 32.5 mag ($\approx 0.05 M_{\odot} \text{ yr}^{-1}$). Given the high-spatial-resolution of the F444W filter ($\sim 0''.15$), the smooth morphology of the extended structure is the direct evidence of the presence of the extended, diffuse ionized gas structure around ID4590. The structure extends towards the radial magnification axis out to $\sim 0''.5$. After the lens correction, this corresponds to ~ 1.7 kpc and at least eight times larger than the rest-frame optical effective radius of ID4590.
5. We perform the optical–mm SED analysis with *HST*, JWST/NIRCcam+MIRI, and ALMA photometry. We exclude the emission outside of the galaxy observed in the F444W filter, and the remaining contribution of the strong emission lines of [O III] $\lambda 5007$ +H β and the stellar continuum is well separated by the rich filter sets of NIRCcam and MIRI. After the lens correction, we estimate the stellar mass of $M_{\text{star}} = 6 \times 10^7 M_{\odot}$, the total star-formation of $\text{SFR} = 3 M_{\odot} \text{ yr}^{-1}$, UV continuum slope of $\beta_{\text{UV}} = -1.7$, suggesting that ID4590 is a low-mass, but a little dust attenuated galaxy, in contrast to very blue galaxies ($\beta_{\text{UV}} < -2.0$) that have been observed in recent *JWST* observations at similar redshifts.
6. Regardless of the ongoing physical mechanisms, past outflow activities are required to make the surrounding pristine gas of ID4590 metal-enriched and produce the [C II] offset and the extended ionized gas structure traced by [O III] $\lambda 5007$ +H β . This would also help produce high ionizing photon escape from ID4590 and contribute to reionization at $z > 8.5$.
7. With careful slit-loss correction and the separation of the emission inside and outside of the

galaxy, we evaluate the electron density of $n_e = 220_{-130}^{+230} \text{ cm}^{-3}$ via the [O III] $88\mu\text{m}$ /[O III] $\lambda 5007$ line ratio. This is much higher than that of local galaxies ($n_e \simeq 30 \text{ cm}^{-3}$), but consistent with $z \sim 2$ –3 galaxies ($n_e \simeq 200 - 300 \text{ cm}^{-3}$). This is also consistent with the upper limit of $n_e < 260 \text{ cm}^{-3}$ obtained in a lensed dusty galaxy at $z = 7.13$.

8. We examine relations between the line luminosities of [C II] $158\mu\text{m}$, [O III] $88\mu\text{m}$, and SFR. ID4590 shows $L_{[\text{CII}]}$ –SFR and $L_{[\text{OIII}]}$ –SFR relations generally consistent with other $z \sim 6$ –9 galaxies and explores the faint-end of the relations, owing to the aid of the lensing support. The $L_{[\text{CII}]}$ /SFR ratio of ID4590 falls below the typical relation estimated among the local dwarf galaxies beyond the errors. Still, it is consistent with similarly metal-poor local galaxies of IZw18 and SBS0335-052. The same result is obtained in the SFR– $L_{[\text{OIII}]}$ relation, while the relation of ID4590 is still consistent with the typical range of the local dwarf galaxies within the errors. ID4590 shows a $L_{[\text{OIII}]}/L_{[\text{CII}]}$ ratio of > 4 , which is also as high as other $z \sim 6$ –9 galaxies, falling above the typical relation of the local dwarf galaxies in the SFR– $L_{[\text{OIII}]}/L_{[\text{CII}]}$ relation.
9. We investigate the physical origins of the high $L_{[\text{OIII}]}/L_{[\text{CII}]}$ ratio with the photoionization model of CLOUDY. The $L_{[\text{OIII}]}$ /SFR– $L_{[\text{CII}]}$ /SFR relation of ID4590 is generally reproduced by the high n_e , low gas-phase metallicity ($Z_{\text{gas}}/Z_{\odot} = 0.04$), high ionization parameter ($\log(U) > -2.27$), and low carbon-to-oxygen abundance ratio $\log(\text{C}/\text{O}) = [-0.52 : -0.24]$ obtained from the *JWST*/NIRSpec data. While the other potential mechanism of the low covering fraction of the photodissociation region is not constrained by the current data, it will be achieved by further deep ALMA [C II] follow-up.

We thank the anonymous referee for constructive comments and suggestions. We also thank Catherine Vlahakis and Holly Sheets for their kind support in the processing of the ALMA data, despite the unusual circumstances due to the cyberattack. We are grateful to Pablo Albalo Halo for sharing deep insights into the NIRSpec data analysis and to Caitlin Casey, Steven Finkelstein, and Daniel Stark for helpful discussions for this paper. This paper makes use of the ALMA data: ADS/JAO. ALMA #2022.A.00022.S. ALMA is a partnership of the ESO (representing its member states), NSF (USA) and NINS (Japan), together with NRC

(Canada), MOST and ASIAA (Taiwan), and KASI (Republic of Korea), in cooperation with the Republic of Chile. The Joint ALMA Observatory is operated by the ESO, AUI/NRAO, and NAOJ. This work is based on observations and archival data made with the *Spitzer Space Telescope*, which is operated by the Jet Propulsion Laboratory, California Institute of Technology, under a contract with NASA, along with archival data from the NASA/ESA *Hubble Space Telescope*. This research also made use of the NASA/IPAC Infrared Science Archive (IRSA), which is operated by the Jet Propulsion Laboratory, California Institute of Technology, under contract with the National Aeronautics and Space Administration. The Early Release Observations¹⁸ and associated materials were developed, executed, and compiled by the ERO production team: Hannah Braun, Claire Blome, Matthew Brown, Margaret Carruthers, Dan Coe, Joseph DePasquale, Nestor Espinoza, Macarena Garcia Marin, Karl Gordon, Alaina Henry, Leah Hustak, Andi James, Ann Jenkins, Anton Koekemoer, Stephanie LaMassa, David Law, Alexandra Lockwood, Amaya Moro-Martin, Susan Mullally, Alyssa Pagan, Dani Player, Klaus Pontoppidan, Charles Proffitt, Christine Pulliam, Leah Ramsay, Swara Ravindranath, Neill Reid, Massimo Robberto, Elena Sabbi, Leonardo Ubeda. The EROs were also made possible by the foundational efforts and support from the JWST instruments, STScI planning and scheduling, and Data Management teams. This project has received funding from the European Union’s Horizon 2020 research and innovation program under the Marie Skłodowska-Curie grant agreement No. 847523 ‘INTERACTIONS’ and from NASA through the NASA Hubble Fellowship grant HST-HF2-51505.001-A awarded by the Space Telescope Science Institute, which is operated by the Association of Universities for Research in Astronomy, Incorporated, under NASA contract NAS5-26555. The project leading to this publication has received support from ORP, that is funded by the European Union’s Horizon 2020 research and innovation programme under grant agreement No 101004719 [ORP]. F.S. acknowledges support from the NRAO Student Observing Support (SOS) award SOSPA7-022. The Cosmic Dawn Center is funded by the Danish National Research Foundation under grant No. 140. K. Kohno acknowledges the support by JSPS KAKENHI Grant Number 17H06130 and the NAOJ ALMA Scientific Research Grant Number 2017-06B. The National Radio Astronomy Observa-

tory is a facility of the National Science Foundation operated under cooperative agreement by Associated Universities, Inc.

Software: CASA (v6.4.1; THE CASA TEAM et al. 2022), *grizli* (Brammer 2023), *EAZY*, (Brammer et al. 2008), *PyNeb* (Shaw et al. 1998) *CLOUDY*, (Ferland et al. 2017), *Interferopy*, (Boogaard et al. 2021b), and *CIGALE* (Boquien et al. 2019) .

¹⁸ <https://www.stsci.edu/jwst/science-execution/approved-programs/webb-first-image-observations>

APPENDIX

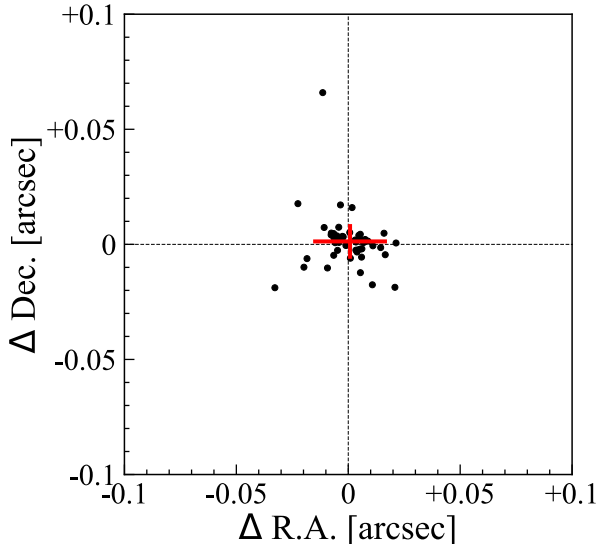


Figure 10. Accuracy of astrometry of the *JWST* and *HST* maps used in our analysis. The black circles show the relative offsets of the coordinates from the GAIA DR3 catalog for the GAIA sources identified in the *JWST* maps, after correcting their proper motion effects. The red cross indicates the average offset, showing excellent agreement with zero. The red cross size corresponds to the standard deviations of $\Delta R.A.$ and $\Delta Dec.$, which we assume as the uncertainty of the positional accuracy for the *JWST* sources (black bar in Figure 2).

A. ACCURACY OF THE ASTROMETRY OF *JWST* AND *HST* MAPS FROM GRIZLI

In Figure 10, we show the residual spatial offsets of the Right ascension ($\Delta R.A.$) and Declination ($\Delta Dec.$) for the GAIA sources. We evaluate the residual offsets by running the SOURCE EXTRACTOR (Bertin & Arnouts 1996) on the *JWST* and *HST* maps produced by the *grizli* pipeline and being corrected for the proper motion effect of the GAIA sources, and comparing with those from the GAIA DR3 catalogs. We confirm that the average offset shows an excellent agreement with zero and the standard deviation in R.A. and Dec. of

$0''.01$ and $0''.02$, respectively. We regard these standard deviations as the positional uncertainty of the *JWST* sources in Figure 2.

B. CIGALE PARAMETERS FOR THE FULL SED FIT

We assume a delayed star-formation history (SFH): $SFR(t) \propto t/\tau^2 \exp(-t/\tau)$ with stellar models from Bruzual & Charlot (2003) and an exponential recent burst implemented in the *sfhdeleyed* module. We use the *dustatt_modified_starburst* module for the dust attenuation, where the nebular emission (continuum + lines) are attenuated with a screen model and an SMC extinction curve (Pei 1992). During the SED fitting, the same $E(B - V)$ is used between stellar and nebular emission. Finally, the dust emission is re-emitted in the infrared with Casey (2012) models. We fix $\beta_d = 1.8$ and the mid-infrared power-law slope $\alpha_d = 2.0$ and adopt the T_d range of 30–90 K. Because no evidence of the presence of AGN has been reported, we do not include an AGN component in the model. We list the modules and the parameter ranges used in the fitting in Table 4. In the fitting, we use the photometry with the 1σ error also for the measurements below the 2σ upper limits. To avoid the lens model uncertainty, we perform the SED fitting with the optical–mm photometry without the lens correction.

C. HST/NIRCAM/MIRI PHOTOMETRY OF ID4590

We summarize the optical–mm photometry used in this paper in Table 5.

D. SIZE MEASUREMENTS

In Figure 11, we summarize the observed, the best-fit model, and the residual maps from the best-fit size measurements for the [C II], [O III], rest-frame UV and optical continuum emission using the ALMA and *JWST*/NIRcam. The methods are described in Section 3.3. We confirm that significant positive and negative pixels remain in the residual maps.

REFERENCES

- Akins, H. B., Fujimoto, S., Finlator, K., et al. 2022, *ApJ*, 934, 64
- Aller, L. H. 1984, *Physics of thermal gaseous nebulae*, doi:10.1007/978-94-010-9639-3
- Andrews, B. H., & Martini, P. 2013, *ApJ*, 765, 140
- Arata, S., Yajima, H., Nagamine, K., Abe, M., & Khochfar, S. 2020, arXiv e-prints, arXiv:2001.01853
- Arellano-Córdova, K. Z., Berg, D. A., Chisholm, J., et al. 2022, arXiv e-prints, arXiv:2208.02562

Parameters	Symbol	Range
Delayed SFH and recent burst		
e-folding time scale of the delayed SFH	τ_{main} [Myr]	100, 250, 500, 1000
Age of the main population	Age_{main} [Myr]	51 log values in [1: 3.3]
Burst	f_{burst}	0.05, 0.10, 0.15, 0.25
SSP		
SSP		BC03
Initial mass function	IMF	Chabrier
Metallicity	Z	0.0004, 0.004, 0.02
Nebular emission		
Ionization parameter	logU	-2.0
Line width [km/s]	—	150
Gas-phase Metallicity	zgas	0.0004, 0.004, 0.02
Electron density	ne	100
Dust attenuation law		
Color excess for both the old and young stellar populations	E_BV_lines	21 log values in [-3: 1.3]
Reduction factor to apply on E_BV_lines to compute E(B-V)s the stellar continuum attenuation	E_BV_factor	1.0
Bump amplitude	uv_bump_amplitude	0.0
Power law slope	power law_slope	0.0
Extinction law to use for attenuating the emission lines flux	Ext_law_emission_lines	SMC
Ratio of total to selective extinction, A_V / E(B-V)	Rv	2.93
Dust emission (Casey2012)		
Dust temperature	temperature	20 log values in [1.5:1.95]
Dust emissivity index	beta	1.8
Mid-infrared power law slope	alpha	2.0
No AGN emission		

Table 4. CIGALE modules and input parameters used for all the fits. BC03 indicates [Bruzual & Charlot \(2003\)](#), and the Chabrier IMF refers to [Chabrier \(2003\)](#).

Table 5. NIR–mm photometry of ID4590 used in this paper

Filter	Flux (nJy)
HST/F105W	-4.7 ± 12.3
HST/F125W	44.5 ± 13.8
HST/F140W	60.5 ± 11.9
HST/F160W	61.7 ± 14.7
NIRCam/F090W	-12.0 ± 3.9
NIRCam/F115W	22.7 ± 8.2
NIRCam/F150W	60.7 ± 6.6
NIRCam/F200W	66.9 ± 7.0
NIRCam/F277W	69.0 ± 7.1
NIRCam/F356W	71.3 ± 7.3
NIRCam/F444W	145.2 ± 14.7
MIRI/F770W	92.2 ± 38.0
MIRI/F1000W	111.2 ± 72.0
MIRI/F1500W	314.1 ± 234.4
MIRI/F1800W	263.9 ± 464.6
ALMA/Band7	$< 41800 (2\sigma)$
ALMA/Band5	$< 23200 (2\sigma)$

NOTE— We adopt the $0''.36$ -diameter aperture photometry corrected to the total flux, where we set an error floor of 10%. The ALMA photometry shows the upper limits at the 2σ level, assuming that the emission is unresolved with the synthesized ALMA beams (FWHM $\sim 0''.7$ in Band 7 and $\sim 1''.3$ in Band 5).

- Atek, H., Shuntov, M., Furtak, L. J., et al. 2022, arXiv e-prints, arXiv:2207.12338
- Bakx, T. J. L. C., Tamura, Y., Hashimoto, T., et al. 2020, MNRAS, 493, 4294
- Behrens, C., Pallottini, A., Ferrara, A., Gallerani, S., & Vallini, L. 2018, MNRAS, 477, 552
- Bertin, E., & Arnouts, S. 1996, A&A, 117, 393
- Bisigello, L., Caputi, K. I., Colina, L., et al. 2019, ApJS, 243, 27
- Boogaard, L., Meyer, R. A., & Novak, M. 2021a, Interferometry: analysing datacubes from radio-to-submm observations, doi:10.5281/ZENODO.5775603
- . 2021b, Interferometry: analysing datacubes from radio-to-submm observations, doi:10.5281/ZENODO.5775603
- Boquien, M., Burgarella, D., Roehlly, Y., et al. 2019, A&A, 622, A103
- Bouwens, R. J., Illingworth, G. D., Ellis, R. S., Oesch, P. A., & Stefanon, M. 2022, arXiv e-prints, arXiv:2205.11526
- Bouwens, R. J., Illingworth, G. D., Oesch, P. A., et al. 2015, ApJ, 803, 34

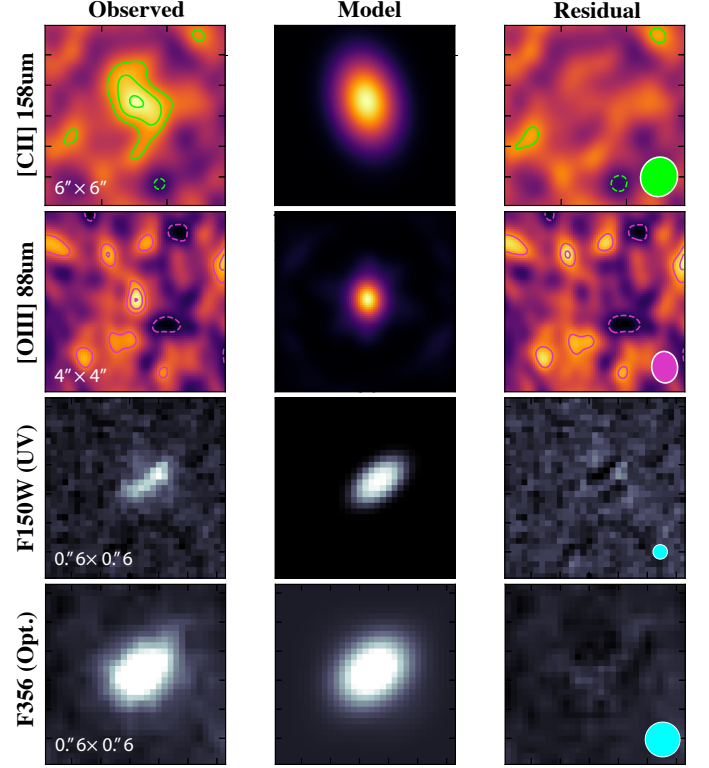


Figure 11. Size measurement results in the image plane. The observed, the best-fit model, and residual (=observed - model) maps are shown from left to right. For the [C II] and [O III] line with ALMA data, we use CASA IMFIT, while for the rest-frame UV and optical continuum with NIRCam/F150W and F356W data, we use GALFIT (Peng et al. 2010). The ellipse (circle) at the bottom right shows the ALMA synthesized beam (NIRCam PSF). Note that IMFIT suggests that [O III] is not spatially resolved, and we use the beam rescaled to the peak of the [O III] line as the best-fit model.

- Bouwens, R. J., Smit, R., Schouws, S., et al. 2021, arXiv e-prints, arXiv:2106.13719
- Bowler, R. A. A., Cullen, F., McLure, R. J., Dunlop, J. S., & Avison, A. 2022, MNRAS, 510, 5088
- Boyer, M. L., Anderson, J., Gennaro, M., et al. 2022, Research Notes of the American Astronomical Society, 6, 191
- Bradley, L. D., Coe, D., Brammer, G., et al. 2022, arXiv e-prints, arXiv:2210.01777
- Brammer, G. 2023, grizli, please cite this software using these metadata., doi:10.5281/zenodo.7767790
- Brammer, G., & Matharu, J. 2021, gbrammer/grizli: Release 2021, Zenodo, doi:10.5281/zenodo.5012699
- Brammer, G. B., van Dokkum, P. G., & Coppi, P. 2008, ApJ, 686, 1503
- Brinchmann, J. 2022, arXiv e-prints, arXiv:2208.07467

- Broadhurst, T., Takada, M., Umetsu, K., et al. 2005, *ApJ*, 619, L143
- Bruzual, G., & Charlot, S. 2003, *MNRAS*, 344, 1000
- Burgarella, D., Buat, V., & Iglesias-Páramo, J. 2005, *MNRAS*, 360, 1413
- Calzetti, D., Armus, L., Bohlin, R. C., et al. 2000, *ApJ*, 533, 682
- Caminha, G. B., Suyu, S. H., Mercurio, A., et al. 2022, *A&A*, 666, L9
- Carnall, A. C., Begley, R., McLeod, D. J., et al. 2023, *MNRAS*, 518, L45
- Carniani, S., Maiolino, R., Pallottini, A., et al. 2017, *A&A*, 605, A42
- Carniani, S., Ferrara, A., Maiolino, R., et al. 2020, *MNRAS*, 499, 5136
- Casey, C. M. 2012, *MNRAS*, 425, 3094
- Chabrier, G. 2003, *PASP*, 115, 763
- Chapin, E. L., Pope, A., Scott, D., et al. 2009, *MNRAS*, 398, 1793
- Charlot, S., & Fall, S. M. 2000, *ApJ*, 539, 718
- Christensen, L., Laursen, P., Richard, J., et al. 2012, *MNRAS*, 427, 1973
- Coe, D., Salmon, B., Bradač, M., et al. 2019, *ApJ*, 884, 85
- Cormier, D., Madden, S. C., Leboutteiller, V., et al. 2015, *Astronomy and Astrophysics*, 578, A53
- Cullen, F., McLure, R. J., McLeod, D. J., et al. 2022, arXiv e-prints, arXiv:2208.04914
- Curti, M., D'Eugenio, F., Carniani, S., et al. 2022, arXiv e-prints, arXiv:2207.12375
- da Cunha, E., Groves, B., Walter, F., et al. 2013, *ApJ*, 766, 13
- Dale, D. A., Helou, G., Magdis, G. E., et al. 2014, *ApJ*, 784, 83
- Davies, R. L., Förster Schreiber, N. M., Genzel, R., et al. 2021, *ApJ*, 909, 78
- De Looze, I., Cormier, D., Leboutteiller, V., et al. 2014, *A&A*, 568, A62
- Díaz-Santos, T., Armus, L., Charmandaris, V., et al. 2017, *ApJ*, 846, 32
- Ellis, R. S., McLure, R. J., Dunlop, J. S., et al. 2013, *ApJ*, 763, L7
- Endsley, R., Stark, D. P., Lyu, J., et al. 2022, arXiv e-prints, arXiv:2206.00018
- Faisst, A. L., Fudamoto, Y., Oesch, P. A., et al. 2020, *MNRAS*, arXiv:2005.07716
- Ferland, G. J., Chatzikos, M., Guzmán, F., et al. 2017, *Rev. Mexicana Astron. Astrofís.*, 53, 385
- Ferrara, A., Pallottini, A., & Dayal, P. 2022, arXiv e-prints, arXiv:2208.00720
- Ferrara, A., Vallini, L., Pallottini, A., et al. 2019, *MNRAS*, 489, 1
- Finkelstein, S. L., Ryan, Russell E., J., Papovich, C., et al. 2015, *ApJ*, 810, 71
- Finkelstein, S. L., Bagley, M. B., Ferguson, H. C., et al. 2023, *ApJ*, 946, L13
- Fudamoto, Y., Inoue, A. K., & Sugahara, Y. 2022a, arXiv e-prints, arXiv:2206.01879
- . 2022b, *ApJ*, 938, L24
- Fudamoto, Y., Oesch, P. A., Faisst, A., et al. 2020, *A&A*, 643, A4
- Fudamoto, Y., Oesch, P. A., Schouws, S., et al. 2021, *Nature*, 597, 489
- Fujimoto, S., Ouchi, M., Ono, Y., et al. 2016, *ApJS*, 222, 1
- Fujimoto, S., Ouchi, M., Ferrara, A., et al. 2019, *ApJ*, 887, 107
- Fujimoto, S., Silverman, J. D., Bethermin, M., et al. 2020, *ApJ*, 900, 1
- Fujimoto, S., Oguri, M., Brammer, G., et al. 2021, *ApJ*, 911, 99
- Fujimoto, S., Brammer, G. B., Watson, D., et al. 2022, *Nature*, 604, 261
- Fujimoto, S., Finkelstein, S. L., Burgarella, D., et al. 2023, *ApJ*, 955, 130
- Furtak, L. J., Shuntov, M., Atek, H., et al. 2022, arXiv e-prints, arXiv:2208.05473
- Gaia Collaboration, Brown, A. G. A., Vallenari, A., et al. 2021, *A&A*, 649, A1
- Giménez-Arteaga, C., Oesch, P. A., Brammer, G. B., et al. 2023, *ApJ*, 948, 126
- Ginolfi, M., Jones, G. C., Béthermin, M., et al. 2020, *A&A*, 633, A90
- Guseva, N. G., Izotov, Y. I., Schaerer, D., et al. 2020, *MNRAS*, 497, 4293
- Harikane, Y., Ouchi, M., Inoue, A. K., et al. 2020, *ApJ*, 896, 93
- Harikane, Y., Inoue, A. K., Mawatari, K., et al. 2022, *ApJ*, 929, 1
- Heintz, K. E., Watson, D., Oesch, P. A., Narayanan, D., & Madden, S. C. 2021, *ApJ*, 922, 147
- Heintz, K. E., Oesch, P. A., Aravena, M., et al. 2022, *ApJ*, 934, L27
- Heintz, K. E., Giménez-Arteaga, C., Fujimoto, S., et al. 2023, *ApJ*, 944, L30
- Herrera-Camus, R., Bolatto, A., Smith, J. D., et al. 2016, *ApJ*, 826, 175
- Herrera-Camus, R., Förster Schreiber, N., Genzel, R., et al. 2021, *A&A*, 649, A31
- Howell, J. H., Armus, L., Mazzarella, J. M., et al. 2010, *ApJ*, 715, 572

- Inami, H., Algera, H. S. B., Schouws, S., et al. 2022, *MNRAS*, 515, 3126
- Inoue, A. K., Hashimoto, T., Chihara, H., & Koike, C. 2020, *MNRAS*, 495, 1577
- Inoue, A. K., Tamura, Y., Matsuo, H., et al. 2016, *Science*, 352, 1559
- Isobe, Y., Ouchi, M., Nakajima, K., et al. 2023a, *ApJ*, 956, 139
- Isobe, Y., Ouchi, M., Tominaga, N., et al. 2023b, *ApJ*, 959, 100
- Jullo, E., Kneib, J. P., Limousin, M., et al. 2007, *New Journal of Physics*, 9, 447
- Kaasinen, M., Bian, F., Groves, B., Kewley, L. J., & Gupta, A. 2017, *MNRAS*, 465, 3220
- Kaasinen, M., van Marrewijk, J., Popping, G., et al. 2022, arXiv e-prints, arXiv:2210.03754
- Kashino, D., Silverman, J. D., Sanders, D., et al. 2017, *ApJ*, 835, 88
- Katz, H., Kimm, T., Sijacki, D., & Haehnelt, M. G. 2017, *MNRAS*, 468, 4831
- Katz, H., Rosdahl, J., Kimm, T., et al. 2022, *MNRAS*, 510, 5603
- Kennicutt, R. C., & Evans, N. J. 2012, *ARA&A*, 50, 531
- Kepley, A. A., Tsutsumi, T., Brogan, C. L., et al. 2020, *PASP*, 132, 024505
- Kewley, L. J., & Dopita, M. A. 2002, *ApJS*, 142, 35
- Kewley, L. J., Nicholls, D. C., Sutherland, R., et al. 2019, *ApJ*, 880, 16
- Killi, M., Watson, D., Fujimoto, S., et al. 2022, arXiv e-prints, arXiv:2211.01424
- Knudsen, K. K., Richard, J., Kneib, J.-P., et al. 2016, *MNRAS*, 462, L6
- Kohandel, M., Ferrara, A., Pallottini, A., et al. 2022, arXiv e-prints, arXiv:2212.02519
- Kohandel, M., Pallottini, A., Ferrara, A., et al. 2020, *MNRAS*, arXiv:2009.05049
- . 2019, *MNRAS*, 487, 3007
- Kojima, T., Ouchi, M., Nakajima, K., et al. 2017, *PASJ*, 69, 44
- Kokorev, V., Brammer, G., Fujimoto, S., et al. 2022, *ApJS*, 263, 38
- Labbe, I., van Dokkum, P., Nelson, E., et al. 2022, arXiv e-prints, arXiv:2207.12446
- Lagache, G., Cousin, M., & Chatzikos, M. 2018, *A&A*, 609, A130
- Lagos, C. d. P., da Cunha, E., Robotham, A. S. G., et al. 2020, *MNRAS*, 499, 1948
- Lambert, T. S., Posses, A., Aravena, M., et al. 2022, *MNRAS*, arXiv:2210.10023
- Le Fèvre, O., Béthermin, M., Faisst, A., et al. 2020, *A&A*, 643, A1
- Lelli, F., Di Teodoro, E. M., Fraternali, F., et al. 2021, *Science*, 371, 713
- Mahler, G., Jauzac, M., Richard, J., et al. 2022, arXiv e-prints, arXiv:2207.07101
- Maiolino, R., & Mannucci, F. 2019, *A&A Rev.*, 27, 3
- Maiolino, R., Carniani, S., Fontana, A., et al. 2015, *MNRAS*, 452, 54
- Martí-Vidal, I., Pérez-Torres, M. A., & Lobanov, A. P. 2012, *A&A*, 541, A135
- Martínez-González, S., Wünsch, R., Silich, S., et al. 2019, *ApJ*, 887, 198
- Mason, C. A., Treu, T., Dijkstra, M., et al. 2018, *ApJ*, 856, 2
- McLure, R. J., Dunlop, J. S., Cullen, F., et al. 2018, *MNRAS*, 476, 3991
- Meurer, G. R., Heckman, T. M., & Calzetti, D. 1999, *ApJ*, 521, 64
- Molyneux, S. J., Smit, R., Schaerer, D., et al. 2022, *MNRAS*, 512, 535
- Naidu, R. P., Oesch, P. A., van Dokkum, P., et al. 2022, *ApJ*, 940, L14
- Nakajima, K., Ouchi, M., Isobe, Y., et al. 2023, *ApJS*, 269, 33
- Nanayakkara, T., Glazebrook, K., Jacobs, C., et al. 2022, arXiv e-prints, arXiv:2207.13860
- Nardiello, D., Bedin, L. R., Burgasser, A., et al. 2022, *MNRAS*, 517, 484
- Nath, B. B., Vasiliev, E. O., Drozdov, S. A., & Shchekinov, Y. A. 2022, arXiv e-prints, arXiv:2211.12378
- Noll, S., Burgarella, D., Giovannoli, E., et al. 2009, *A&A*, 507, 1793
- Oesch, P. A., Brammer, G., van Dokkum, P. G., et al. 2016, *ApJ*, 819, 129
- Oguri, M. 2010, *PASJ*, 62, 1017
- . 2021, *PASP*, 133, 074504
- Ono, Y., Harikane, Y., Ouchi, M., et al. 2022, arXiv e-prints, arXiv:2208.13582
- Ota, K., Walter, F., Ohta, K., et al. 2014, *ApJ*, 792, 34
- Pallottini, A., Gallerani, S., Ferrara, A., et al. 2015, *MNRAS*, 453, 1898
- Pallottini, A., Ferrara, A., Decataldo, D., et al. 2019, *MNRAS*, 487, 1689
- Pallottini, A., Ferrara, A., Gallerani, S., et al. 2022, *MNRAS*, 513, 5621
- Papovich, C., Cole, J. W., Yang, G., et al. 2023, *ApJ*, 949, L18
- Pascale, M., Frye, B. L., Diego, J., et al. 2022, *ApJ*, 938, L6
- Pei, Y. C. 1992, *ApJ*, 395, 130

- Peng, C. Y., Ho, L. C., Impey, C. D., & Rix, H.-W. 2010, *AJ*, 139, 2097
- Pilyugin, L. S., & Thuan, T. X. 2005, *ApJ*, 631, 231
- Pilyugin, L. S., Vílchez, J. M., Mattsson, L., & Thuan, T. X. 2012, *MNRAS*, 421, 1624
- Pizzati, E., Ferrara, A., Pallottini, A., et al. 2020, arXiv e-prints, arXiv:2001.10547
- Planck Collaboration, Abergel, A., Ade, P. A. R., et al. 2011, *A&A*, 536, A21
- Pontoppidan, K., Blome, C., Braun, H., et al. 2022, arXiv e-prints, arXiv:2207.13067
- Popping, G. 2022, arXiv e-prints, arXiv:2208.13072
- Reddy, N. A., Oesch, P. A., Bouwens, R. J., et al. 2018, *ApJ*, 853, 56
- Rizzo, F., Vegetti, S., Powell, D., et al. 2020, *Nature*, 584, 201
- Robertson, B. E., Tacchella, S., Johnson, B. D., et al. 2022, arXiv e-prints, arXiv:2212.04480
- Romano, M., Cassata, P., Morselli, L., et al. 2020, *MNRAS*, 496, 875
- Rossa, J., & Dettmar, R. J. 2000, *A&A*, 359, 433
- . 2003, *A&A*, 406, 505
- Sanders, R. L., Shapley, A. E., Kriek, M., et al. 2016, *ApJ*, 816, 23
- Sanders, R. L., Shapley, A. E., Reddy, N. A., et al. 2020, *MNRAS*, 491, 1427
- Schaerer, D., Marques-Chaves, R., Oesch, P., et al. 2022, arXiv e-prints, arXiv:2207.10034
- Schaerer, D., Ginolfi, M., Béthermin, M., et al. 2020, *A&A*, 643, A3
- Shaw, R. A., de La Pena, M. D., Katsanis, R. M., & Williams, R. E. 1998, in *Astronomical Society of the Pacific Conference Series*, Vol. 145, *Astronomical Data Analysis Software and Systems VII*, ed. R. Albrecht, R. N. Hook, & H. A. Bushouse, 192
- Smit, R., Bouwens, R. J., Carniani, S., et al. 2018, *Nature*, 553, 178
- Sommovigo, L., Ferrara, A., Carniani, S., et al. 2022a, *MNRAS*, 517, 5930
- Sommovigo, L., Ferrara, A., Pallottini, A., et al. 2022b, *MNRAS*, 513, 3122
- Spilker, J. S., Aravena, M., Béthermin, M., et al. 2018, *Science*, 361, 1016
- Stark, D. P., Ellis, R. S., Charlot, S., et al. 2017, *MNRAS*, 464, 469
- Steidel, C. C., Rudie, G. C., Strom, A. L., et al. 2014, *ApJ*, 795, 165
- Stott, J. P., Swinbank, A. M., Johnson, H. L., et al. 2016, *MNRAS*, 457, 1888
- Sugahara, Y., Inoue, A. K., Fudamoto, Y., et al. 2022, *ApJ*, 935, 119
- Sun, F., Egami, E., Fujimoto, S., et al. 2022, arXiv e-prints, arXiv:2204.07187
- Swinbank, A. M., Simpson, J. M., Smail, I., et al. 2014, *MNRAS*, 438, 1267
- Tacchella, S., Johnson, B. D., Robertson, B. E., et al. 2022, arXiv e-prints, arXiv:2208.03281
- Tadaki, K., Iono, D., Yun, M. S., et al. 2018, *Nature*, 560, 613
- THE CASA TEAM, Bean, B., Bhatnagar, S., et al. 2022, arXiv e-prints, arXiv:2210.02276
- Topping, M. W., Stark, D. P., Endsley, R., et al. 2022a, arXiv e-prints, arXiv:2208.01610
- . 2022b, *MNRAS*, 516, 975
- Trump, J. R., Arrabal Haro, P., Simons, R. C., et al. 2022, arXiv e-prints, arXiv:2207.12388
- Tsukui, T., & Iguchi, S. 2021, *Science*, 372, 1201
- Valentino, F., Brammer, G., Fujimoto, S., et al. 2022, *ApJ*, 929, L9
- Vallini, L., Ferrara, A., Pallottini, A., Carniani, S., & Gallerani, S. 2020, *MNRAS*, 495, L22
- . 2021, *MNRAS*, 505, 5543
- Vallini, L., Gallerani, S., Ferrara, A., Pallottini, A., & Yue, B. 2015, *ApJ*, 813, 36
- Watson, D., Christensen, L., Knudsen, K. K., et al. 2015, *Nature*, 519, 327
- Witstok, J., Smit, R., Maiolino, R., et al. 2022, *MNRAS*, 515, 1751
- Zhang, Z.-Y., Papadopoulos, P. P., Ivison, R. J., et al. 2016, *Royal Society Open Science*, 3, 160025
- Ziparo, F., Ferrara, A., Sommovigo, L., & Kohandel, M. 2022, arXiv e-prints, arXiv:2209.06840
- Zitrin, A., Broadhurst, T., Umetsu, K., et al. 2009, *MNRAS*, 396, 1985
- Zitrin, A., Fabris, A., Merten, J., et al. 2015, *ApJ*, 801, 44
- Zurita, A., Rozas, M., & Beckman, J. E. 2000, *A&A*, 363, 9